

JGR Solid Earth

RESEARCH ARTICLE

10.1029/2023JB028280

Special Section:

Advances in understanding volcanic processes

Key Points:

- Seismic wave radiation through ring fault and magma, as well as high magma viscosity, reduce fault slip by up to half during collapse
- Rupture propagation, downward momentum transfer via magma pressure waves, and chamber pressurization are identified in unfiltered seismograms
- Comparison between simulated and observed near-field seismograms from Kīlauea 2018 reveals complex nucleation phase on the ring fault

Supporting Information:

Supporting Information may be found in the online version of this article.

Correspondence to:

T. A. Wang,
taiyi@stanford.edu

Citation:

Wang, T. A., Dunham, E. M., Krenz, L., Abrahams, L. S., Segall, P., & Yoder, M. R. (2024). Dynamic rupture simulations of caldera collapse earthquakes: Effects of wave radiation, magma viscosity, and evidence of complex nucleation at Kīlauea 2018. *Journal of Geophysical Research: Solid Earth*, 129, e2023JB028280. <https://doi.org/10.1029/2023JB028280>

Received 15 NOV 2023

Accepted 5 MAR 2024

Author Contributions:

Conceptualization: Taiyi A. Wang, Eric M. Dunham

Data curation: Taiyi A. Wang, Eric M. Dunham

Formal analysis: Taiyi A. Wang, Eric M. Dunham

Funding acquisition: Eric M. Dunham, Paul Segall

Investigation: Taiyi A. Wang, Eric M. Dunham, Lukas Krenz, Paul Segall

Methodology: Taiyi A. Wang, Eric M. Dunham, Lukas Krenz, Lauren S. Abrahams, Paul Segall

© 2024. American Geophysical Union. All Rights Reserved.

Dynamic Rupture Simulations of Caldera Collapse Earthquakes: Effects of Wave Radiation, Magma Viscosity, and Evidence of Complex Nucleation at Kīlauea 2018

Taiyi A. Wang¹ , Eric M. Dunham^{1,2} , Lukas Krenz³ , Lauren S. Abrahams⁴ , Paul Segall¹ , and Mark R. Yoder⁵

¹Department of Geophysics, Stanford University, Stanford, CA, USA, ²Institute for Computational and Mathematical Engineering, Stanford University, Stanford, CA, USA, ³Department of Informatics, Technical University of Munich, Munich, Germany, ⁴Lawrence Livermore National Laboratory, Livermore, CA, USA, ⁵Stanford Research Computing, Stanford, CA, USA

Abstract All instrumented basaltic caldera collapses have generated $M_w > 5$ very long period earthquakes. However, previous studies of source dynamics have been limited to lumped models treating the caldera block as rigid, leaving open questions related to how ruptures initiate and propagate around the ring fault, and the seismic expressions of those dynamics. We present the first 3D numerical model capturing the nucleation and propagation of ring fault rupture, the mechanical coupling to the underlying viscoelastic magma, and the associated seismic wavefield. We demonstrate that seismic radiation, neglected in previous models, acts as a damping mechanism reducing coseismic slip by up to half, with effects most pronounced for large magma chamber volume/ring fault radius or highly compliant crust/compressible magma. Viscosity of basaltic magma has negligible effect on collapse dynamics. In contrast, viscosity of silicic magma significantly reduces ring fault slip. We use the model to simulate the 2018 Kīlauea caldera collapse. Three stages of collapse, characterized by ring fault rupture initiation and propagation, deceleration of the downward-moving caldera block and magma column, and post-collapse resonant oscillations, in addition to chamber pressurization, are identified in simulated and observed (unfiltered) near-field seismograms. A detailed comparison of simulated and observed displacement waveforms corresponding to collapse earthquakes with hypocenters at various azimuths of the ring fault reveals a complex nucleation phase for earthquakes initiated on the northwest. Our numerical simulation framework will enhance future efforts to reconcile seismic and geodetic observations of caldera collapse with conceptual models of ring fault and magma chamber dynamics.

Plain Language Summary Caldera collapse manifests as the rapid subsidence of a kilometer-scale block of crust circumscribed by a near-circular fault on top of a volcano. The subsidence of the caldera block is caused by the eruption-induced withdrawal of magma and reduction in pressure in the underlying magma chamber. All scientifically instrumented caldera collapses at volcanoes with low-viscosity magma are accompanied by earthquakes of magnitude 5 and above. How do magma viscosity and the seismic wave radiation influence the amount of slip per earthquake on the fault? What can we learn about the dynamics of these earthquakes from seismic records? We address these questions by performing computer simulations of caldera collapse earthquakes and compare the results to the seismic records from the Kīlauea caldera collapse of 2018.

1. Introduction

Basaltic caldera collapse initiates when the crust overlying a magma chamber fails catastrophically due to eruption-induced magma chamber pressure decrease. Over the course of a few months, the subsidence of the crust (“caldera block”) is accommodated by episodic, meter-scale slip on a near-circular fault (“ring fault”) kilometers in diameter, with collapse slip events having recurrence intervals of hours to days (Geshi et al., 2002; Gudmundsson et al., 2016; Neal et al., 2019; Peltier et al., 2009). These ring fault slip events manifest as $M_w > 5$ very long period (VLP) earthquakes (Duputel & Rivera, 2019; Fontaine et al., 2019; Gudmundsson et al., 2016; Kumagai et al., 2001; Lai et al., 2021; Wang et al., 2022) at every instrumented basaltic caldera collapse (Miyakejima 2001, Piton de la Fournaise, 2007, Bárðarbunga 2014, Kīlauea 2018). In addition to the flank eruptions sustained by collapse earthquakes (Dietterich et al., 2021; Patrick et al., 2019; Roman & Lundgren, 2021; Segall & Anderson, 2021), the earthquakes pose significant hazards to the region surrounding the

Resources: Eric M. Dunham, Lukas Krenz, Paul Segall, Mark R. Yoder
Software: Taiyi A. Wang, Lukas Krenz, Lauren S. Abrahams, Mark R. Yoder
Supervision: Eric M. Dunham, Paul Segall
Validation: Taiyi A. Wang, Eric M. Dunham, Paul Segall
Visualization: Taiyi A. Wang, Eric M. Dunham, Lauren S. Abrahams
Writing – original draft: Taiyi A. Wang
Writing – review & editing: Taiyi A. Wang, Eric M. Dunham, Lukas Krenz, Lauren S. Abrahams, Paul Segall

volcano (Williams et al., 2020). Therefore, it is critical to understand the mechanics of caldera collapse earthquakes.

Caldera collapse earthquakes are inherently 3D processes with spatial-temporal variations in slip and stress. Much like earthquakes on tectonic faults, caldera collapse earthquakes must nucleate at a high-stress or low-strength region on the ring fault. Once the rupture expands past a critical nucleation dimension, it propagates dynamically around the ring fault, as indicated by seismic source inversions (Fichtner & Tkalčić, 2010). It is not until the rupture fronts converge on the opposite side of the ring fault when slip occurs *everywhere simultaneously*, a condition implicit in lumped parameter models of caldera collapse earthquakes (Gudmundsson et al., 2016; Kumagai et al., 2001; Roman & Lundgren, 2021; Segall & Anderson, 2021; Wang et al., 2022). Nonetheless, lumped models brought tremendous insights into critical questions regarding the mechanics of caldera collapse earthquakes, such as: why are caldera collapse earthquakes unexpectedly long-duration and large-magnitude, compared to tectonic earthquakes on faults of similar sizes? The long slip duration is the reason that collapse earthquakes manifest as VLP earthquakes (seismic corner frequency shifts lower with longer slip duration; e.g., Savage (1972)). The large slip magnitude is the reason that collapse earthquakes sustain chamber overpressure over month-long eruptions (each collapse earthquake reduces chamber volume and increases chamber pressure; e.g., Segall and Anderson (2021)).

In the following, we explicitly address these questions and motivate for 3D dynamic rupture simulations. The puzzling questions are clearly embodied when comparing the observations from the caldera collapse earthquakes at Kīlauea in 2018, the best monitored caldera collapse in history (K. R. Anderson et al., 2023), with the following scaling of tectonic earthquakes. Consider rupture propagation on a rectangular normal fault. Because the ring fault at Kīlauea summit is nearly vertical (Segall et al., 2020), we assume that the fault has a down-dip dimension, L , equivalent to the height of the caldera block, defined as the distance from the summit surface to the top of the magma reservoir. The fault has an along-strike dimension, $2\pi R$, equivalent to the circumference of a ring fault with radius R . For $2\pi R \gg L$, the rupture duration (defined as the time between dynamic slip initiation and cessation everywhere on the fault), T , is approximately

$$T \approx \frac{2\pi R}{v_r}, \quad (1)$$

where v_r is the rupture velocity. The slip magnitude, S , is approximately (Day, 1982; Madariaga, 1976)

$$S \approx \frac{L}{C\mu_r} \Delta\tau, \quad (2)$$

where μ_r is the crustal shear modulus, $\Delta\tau$ the coseismic stress drop, and $C \in [0.65, 2.55]$ is a non-dimensional shape factor.

At Kīlauea, the height of the caldera block, L , and average ring fault radius, R , are approximately 1 km (K. Anderson et al., 2019). The average S-wave speed for the upper 1 km of crust is approximately 1.7 km s⁻¹ (Dawson et al., 1999; Lin et al., 2014; Saccorotti et al., 2003). Assuming that ring fault rupture occurs at the Rayleigh wave speed (approximately 90% of S-wave speed), we estimate T of 4 s. However, both GNSS (Global Navigation Satellite System) time series (K. Anderson & Johanson, 2022) and VLP seismic waveforms (Lai et al., 2021; Wang et al., 2022) indicate a rupture duration up to 10 s for collapse earthquakes in late June and July, 2018, when the ring fault was fully developed (K. R. Anderson et al., 2023). Assuming $C = 1$, $\mu_r = 7.8$ GPa (for typical basaltic rock density of 2.7×10^3 kg m⁻³ and aforementioned S-wave speed), and $\Delta\tau = 1$ MPa (Segall & Anderson, 2021), we estimate S of 0.1 m, which is an order of magnitude smaller than the GNSS-derived average coseismic slip of 2–5 m (K. Anderson & Johanson, 2022; Tepp et al., 2020). To reconcile the large discrepancy in observed and theoretical estimates of T and S , anomalously low μ_r , inconsistent with observed seismic wave speeds, would be required.

The discrepancy between theory and observation is resolved by recognizing that, after *earthquake nucleation*, caldera collapse earthquakes are comprised of a *rupture phase*, the period in between the onset of dynamically propagating fault rupture and the simultaneous slip of the entire fault, as well as a *collapse phase*, the period in between the onset of simultaneous slip of the entire fault and the cessation of slip everywhere on the fault. The

collapse phase is characterized by the mechanical coupling between fault slip and the underlying magma chamber. When wave radiation effects are negligible, or $\omega\mathcal{L}/c \ll 1$ (ω , c : characteristic angular frequency of waves and wave speed, respectively; \mathcal{L} : characteristic dimension of the source), a lumped model with axisymmetric slip on a vertical ring fault, accounting for caldera block/magma momentum balance, chamber pressurization, and ring fault stress drop, yields a new scaling (Gudmundsson et al., 2016; Kumagai et al., 2001; Roman & Lundgren, 2021; Segall & Anderson, 2021; Wang et al., 2022):

$$T_{col} \approx \frac{1}{R^2} \sqrt{\beta V m'}, \quad (3)$$

$$S_{col} \approx \frac{4\beta V L \Delta\tau}{\pi R^3}, \quad (4)$$

$$m' = m + \phi m_f, \quad (5)$$

where β is the total compressibility of the magma reservoir (magma + chamber), V the chamber volume, m the mass of the caldera block, m_f the mass of magma in the reservoir, and ϕ the fraction of total magma mass acting as inertial mass impeding caldera block motion. For a vertically oriented cylindrical magma chamber with the same radius as the caldera block, $\phi = 1/3$ (Wang et al., 2022).

We identify T_{col} and S_{col} as the duration and slip magnitude during the collapse phase, respectively. For typical crustal elastic moduli and chamber compressibility in volcanic environments, the duration of the rupture phase, T , is always small compared to that of the subsequent collapse phase, T_{col} , unless $R/\sqrt{HL} \geq 1$ (H is the vertical dimension of the chamber). The magnitude of ring fault slip is proportional to the compressibility of the chamber, which, for basaltic magma containing exsolved volatiles, is typically dominated by magma compressibility (with the exception of dike or sill like chambers). For Kīlauea, appropriate parameter values for Equations 3 and 4 are: $R = 1$ km, $\beta = 7 \times 10^{-10}$ Pa⁻¹, $V = 4$ km³, $L = 1$ km, and $\Delta\tau = 1$ MPa (K. Anderson et al., 2019; Segall & Anderson, 2021; Wang et al., 2022). Assuming $\phi = 1/3$, magma density $\rho_m = 2.6 \times 10^3$ kg m⁻³, and rock density $\rho_r = 2.7 \times 10^3$ kg m⁻³, we have $m = \pi R^2 L \rho_r \approx 8.5 \times 10^{12}$ kg and $m_f = V \rho_m \approx 10^{13}$ kg. The predicted T_{col} and S_{col} are 6 s and 4 m, respectively, consistent with observations. Therefore, caldera collapse earthquakes have longer than expected duration due to the collapse duration (Equation 3) being much longer than the rupture duration (Equation 1). Caldera collapse earthquakes incur larger than expected ring fault slip, mainly due to the fact that slip is proportional to magma compressibility (Equation 4) instead of crustal compressibility (Equation 2).

Here we seek a deeper understanding of factors controlling the duration and magnitude of fault slip during caldera collapse earthquakes. Lumped models assume uniform slip on the ring fault, therefore neglecting the rupture phase and only appropriate for modeling the collapse phase. Further, lumped models neglect seismic wave radiation and assume inviscid magma. As we will show, neglecting wave radiation effects is invalid for caldera systems with large spatial dimensions, slow wave propagation in compressible magma or surrounding compliant crust. Inviscid assumption for fluid is reasonable for basaltic magma, but invalid for silicic magma.

In this study, we systematically investigate the physics of caldera collapse earthquakes, eliminating the above assumptions with numerical dynamic rupture simulations and complementary analytical analyses. Additionally, we make theoretical predictions of the surface wavefield for realistic caldera collapse scenarios, gaining insight into rupture nucleation, propagation, and magma chamber responses to collapse. The paper is organized as follows. In Section 2, we introduce a numerical simulation method for caldera collapse earthquakes using SeisSol (Dumbser et al., 2007; Krenz et al., 2021; Ulrich et al., 2022; Uphoff & Bader, 2016), a discontinuous Galerkin finite element code for earthquake rupture dynamics and seismic wave propagation. The simulation can capture the nucleation and propagation of rupture on the ring fault, as well as the wavefield in the solid crust, basaltic magma (approximated as an inviscid acoustic fluid with zero shear modulus), and silicic magma (approximated as a linear Maxwell viscoelastic material, in which shear waves and deviatoric stresses are relaxed by viscous flow). In Section 3, we investigate the influence of wave radiation and magma viscosity on the duration and magnitude of ring fault slip. In Section 4, we perform a dynamic rupture simulation with relevant chamber, ring fault geometry and material properties for the 2018 caldera collapse of Kīlauea. We compare simulated near-field waveforms with observations to identify phases of earthquake nucleation, rupture propagation, deceleration of the downward-moving caldera block and magma column, and post-collapse resonant oscillations.

2. Simulation Method

We introduce two categories of 3D simulations with distinct chamber and ring fault geometries, magmatic and crustal material properties, and initial stress conditions. “Benchmark case” simulations are performed to isolate the effect of seismic radiation and magma viscosity on ring fault slip magnitude and duration (Section 3). “Kīlauea case” simulations are performed to guide interpretations of near-field seismic waveforms at Kīlauea in 2018 (Section 4). In both cases, the ring fault is loaded with shear tractions in the down-dip direction to emulate stress conditions resulting from a pressure deficit in the magma chamber.

For the benchmark case, the crust is set up for linear elastodynamics with homogeneous, isotropic moduli, except the volume occupied by magma, the constitutive law of which is discussed below. For the Kīlauea case, we utilize a 1D (depth-dependent) elastic property model with attenuation. For both cases, we assume slip weakening friction on the ring fault. This is a reasonable approximation since we do not seek to simulate episodic collapses. During fault slip, the friction coefficient, f , decreases linearly from a static value, f_s , to a dynamic value, f_d , over a slip weakening distance, D_c , and remains constant for slip beyond D_c . For the benchmark case, fault strength is defined as $f\sigma$, where σ is normal stress. For the Kīlauea case, fault strength $f\sigma + C$ additionally includes cohesion, C .

Magma is a multi-phase fluid with crystal, melt, and volatile phases. Here we are concerned with the bulk mechanical properties of magma at time scales relevant to caldera collapse earthquakes and model magma as a homogeneous material. Magma is viscoelastic in nature (e.g., Webb & Dingwell, 1990), with the elastic and viscous regimes for deviatoric straining demarcated by its intrinsic relaxation time scale(s). We assume that magma is well approximated by a Maxwell viscoelastic material with deviatoric stresses relaxing toward zero over a single relaxation time, τ_M (defined as the ratio of dynamic viscosity, η_m , to magma shear modulus, μ_m). This material permits transmission of attenuated shear waves at $\omega\tau_M \gg 1$, and forbids transmission of shear waves at $\omega\tau_M \ll 1$ (here ω denotes the angular frequency of shear waves).

For silicate melts, τ_M varies over orders of magnitude due to large variability of η_m and a relatively constant μ_m (Dingwell & Webb, 1989). At storage temperatures ($\geq 1100^\circ\text{C}$), basaltic magma has $\mu_m \sim 1 \text{ GPa}$ (James et al., 2004), and $\eta_m \sim 10^2 \text{ Pa s}$ (Pinkerton & Norton, 1995), corresponding to $\tau_M \sim 10^{-7} \text{ s} \ll T_{\text{col}}$, indicating that elastic behavior can be neglected for deviatoric straining. For silicic magma with low vesicularity at storage temperatures ($\geq 650^\circ\text{C}$), $\mu_m \sim 10^{-2} - 10^{-1} \text{ GPa}$, and $\eta_m \sim 10^8 \text{ Pa s}$ (Okumura et al., 2010). These values correspond to $\tau_M = 1-10 \text{ s}$, indicating that viscoelastic behavior should be considered. Furthermore, viscous drag forces from magma can influence ring fault slip only when the ratio of magmatic boundary layer thickness near the chamber wall, L_{boundary} , to the characteristic dimension of the chamber, approaches unity. As shown in Section 3.1, for an idealized cylindrical chamber with radius R , $L_{\text{boundary}}/R \sim 10^{-3}$ for basaltic magma and $L_{\text{boundary}}/R \sim 10^{-1}$ for silicic magma. This indicates that basaltic magma is expected to behave like a compressible, inviscid fluid and silicic magma a compressible, viscoelastic fluid during caldera collapse earthquakes.

Therefore, we model basaltic magma as an acoustic fluid (a built-in option in SeisSol), which has zero viscosity. We model silicic magma as a Maxwell material, achieved by utilizing the memory variable attenuation feature of SeisSol using the procedure described in Appendix A. The method can be generalized to approximate arbitrarily complex linear viscoelastic rheology with multiple relaxation times.

3. Control on Collapse Duration and Magnitude

Here we investigate the effects of magma viscosity and seismic wave radiation on the duration and magnitude of ring fault slip during caldera collapse earthquakes. The effect of magma viscosity is qualitatively shown to reduce slip magnitude via a pair of benchmark case simulations with different magma rheologies. The effect of wave radiation through the caldera block/magma interface is quantified via a parameter study using the benchmark case simulations, and shown to reduce fault slip. Further physical intuition on the effect of wave radiation through the ring fault on collapse dynamics is gained using asymptotic solutions for impedance (ratio of stress change to fault slip rate) for an idealized 2D antiplane shear ring fault in an isotropic and linear elastodynamic full space.

All benchmark case simulations adopt idealized geometries for the ring fault and chamber, and assume axisymmetric rupture on the ring fault (Figure 1a). This is done to isolate features associated with collapse, without the additional complexities associated with ring fault rupture propagation. The magma chamber is a

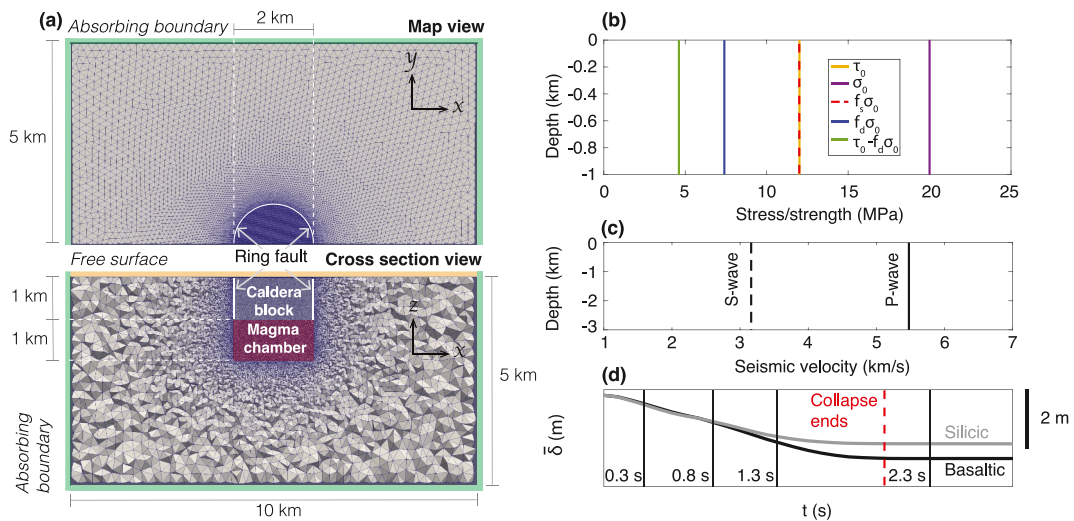


Figure 1. (a) 3D simulation setup for the benchmark case showing tetrahedral mesh, boundary conditions, and caldera geometry. For simplicity, both caldera block and underlying magma chamber are cylindrical. (b) Initial conditions on fault stress and strength. τ_0 , σ_0 , f_s , f_d : initial shear, normal stresses, and static, dynamic friction coefficients. (c) Velocity model for the crust. Note that for the parameter study investigating the effect of wave radiation, magma is modeled as a compressible fluid with zero viscosity and shear modulus. Magma chamber vertical dimension varies from 1 to 6 km and magma compressibility varies between 1×10^{-10} and $7.4 \times 10^{-10} \text{ Pa}^{-1}$. (d) Spatially averaged slip, $\bar{\delta}$, on the ring fault for the simulations with basaltic and silicic magmas, with vertical lines indicating the timing of wavefield snapshots in Figures 2 and 3.

vertical cylinder with the same cross-sectional radius as the overlying caldera block, which is bounded by a vertical, cylindrical ring fault. Ring fault rupture is initiated with a spatially uniform downward shear traction slightly higher than the spatially uniform shear strength (Figure 1b; Table 1). The crustal elastic moduli are such that the chamber wall is stiff (Figure 1c; Table 1) and the subsidence of the caldera block into the chamber induces

Table 1
Model Parameters for Simulations

Parameter	Symbol	Benchmark case	Kilauea case	Unit
<i>Crust</i>				
Density	ρ_r	3,000	2,700	kg m^{-3}
Shear modulus	μ_r	30	1D velocity model with attenuation ^a	GPa
Poisson's ratio	ν	0.25	0.25	
<i>Magma</i>				
Density	ρ_m	2,700	2,600	kg m^{-3}
Shear modulus ^b	μ_m	0 for basaltic magma; 0.01 for silicic magma	0	GPa
Compressibility	β_m	0.1	0.46 ^c	GPa^{-1}
Viscosity ^b	η_m	0 for basaltic magma; 100 for silicic magma	0	$\text{MPa} \cdot \text{s}$
<i>Fault</i>				
Static friction	f_s	0.6	0.61 outside of nucleation patch; 0.59 inside of nucleation patch	
Dynamic friction	f_d	0.37	0.53	
Slip evolution distance	D_c	1	1	cm
Cohesion	C	0	0.2	MPa
Initial shear stress	τ_0	12.01	Depth dependent ^d	MPa
Initial normal stress	σ_0	20	Depth dependent ^d	MPa

^aSee Figure 7c. ^bThese are target values approximated with the procedure described in Appendix A. ^cMedian value estimated by K. Anderson et al. (2019). ^dSee Figure 7b.

relatively small shear strength changes on the ring fault, as compared to shear stress changes, facilitating comparison with analytical solutions of lumped models. All domain boundaries, except the free surface, are absorbing boundaries, where wave reflections are minimized. The timing of wavefield snapshots in Section 3.1 are marked along the spatially averaged ring fault slip history (Figure 1d).

3.1. Magma Viscosity

We compare basaltic and silicic benchmark case simulations to discern the effect of magma viscosity on ring fault slip. An example simulation (Figure 2) is shown for basaltic magma with minimal exsolved volatiles (parameters in Table 1). At 0.3 s, the caldera block accelerates downward, setting off elastic rebound outside of the ring fault and downward propagating P-waves in the magma (Figure 2a). The apparent reversed sense of polarity at wave fronts along earth surface (upward inside of the ring fault and downward outside of the ring fault) is attributed to precursory body waves preceding Rayleigh waves in Lamb's problem (Mooney, 1974). Between 0.8 and 1.3 s, the caldera block and the magma column decelerate due to chamber pressure increase, resulting in the transmission of downward momentum from the caldera block and magma into the surrounding crust. This manifests as downward velocity of the crust outside of the ring fault (Figures 2b and 2c). At 2.3 s, ring fault slip stops (Figure 2d). The caldera block (in conjunction with surrounding crust) and the magma inside the chamber move upwards due to the conversion of elastic strain energy stored in the crust and magma back to kinetic energy. Hereafter, oscillations due to elastic strain energy and kinetic energy conversions continue for tens of seconds.

With silicic magma, we expect the viscous drag on the descending magma to transfer some of the downward momentum laterally out into the crust through boundary layer development, reducing the slip rate on the ring fault. The effect can be quantified through the ratio of lateral momentum transfer through viscous boundary layer, $\Delta P_{viscous}$, to total momentum residing in the magma prior to boundary layer development, P_{total} . For a cylindrical chamber with cross-sectional radius, $R \sim 10^3$ m, chamber height, H , and spatially averaged magma flow velocity (mostly in the vertical direction), $v \sim 1$ m s⁻¹, the Reynolds number during caldera collapse, $\rho_m v R / \eta_m$, is of order $10^{-2} - 10^1$, indicating that flow is within the laminar regime (the Reynolds number for basaltic magma is $10^3 - 10^4$, at the upper end of the laminar regime). Thus $L_{boundary}$ scales as $\sqrt{\nu_m T_{col}}$, where $\nu_m = \eta_m / \rho_m$ is the kinematic viscosity, and the spatially averaged viscous traction along the chamber side walls, $\Delta \tau_{rz}$, scales as $\eta_m v / \sqrt{\nu_m T_{col}}$. $\Delta P_{viscous}$ can be obtained via time integral of the lateral momentum transfer rate, $2\pi R H \Delta \tau_{rz}$:

$$\Delta P_{viscous} = \int_0^{T_{col}} 2\pi R H \Delta \tau_{rz} dt \sim 2\pi R H \eta_m v \sqrt{\frac{T_{col}}{\nu_m}}. \quad (6)$$

The total vertical momentum residing in the magma prior to boundary layer development is

$$P_{total} = \pi R^2 H \rho_m v. \quad (7)$$

Therefore, the momentum ratio is

$$\frac{\Delta P_{viscous}}{P_{total}} \sim \frac{2\sqrt{\nu_m T_{col}}}{R} \sim \frac{L_{boundary}}{R}. \quad (8)$$

At the time scale of collapse earthquakes ($T_{col} \sim 10$ s), $L_{boundary} \sim 10^2$ m and $L_{boundary}/R \sim 10^{-1}$ for silicic magma, allowing for reduction in vertical motion of the caldera block. In contrast, $L_{boundary} \sim 1$ m and $L_{boundary}/R \sim 10^{-3}$ for basaltic magma. Thus boundary layers have little effect on basaltic collapse dynamics.

Next we show the development of boundary layers in a simulation (Figure 3) for silicic magma with minimal exsolved volatiles (parameters in Table 1). The magma has a viscosity of 10^8 Pa s and a shear modulus of 10^7 Pa, with a corresponding Maxwell relaxation time, τ_M , of 10 s. Compared to the basaltic simulation, the silicic simulation shows viscous boundary layer development along the vertical chamber walls (Figures 3a–3c). The boundary layers grow wider as the caldera block continues to drive downward flow in the chamber, imparting downward momentum into the surrounding crust. By 1.3 s, the boundary layer on either side of the chamber wall reaches a mean thickness of 0.2 km (Figures 3e and 3f). Drag on the magma is exemplified by viscous deviatoric stress $\Delta \sigma_{rz} \approx 1$ MPa near the chamber wall (region 1 and 2 in Figure 4a), which arises due to high viscous strain

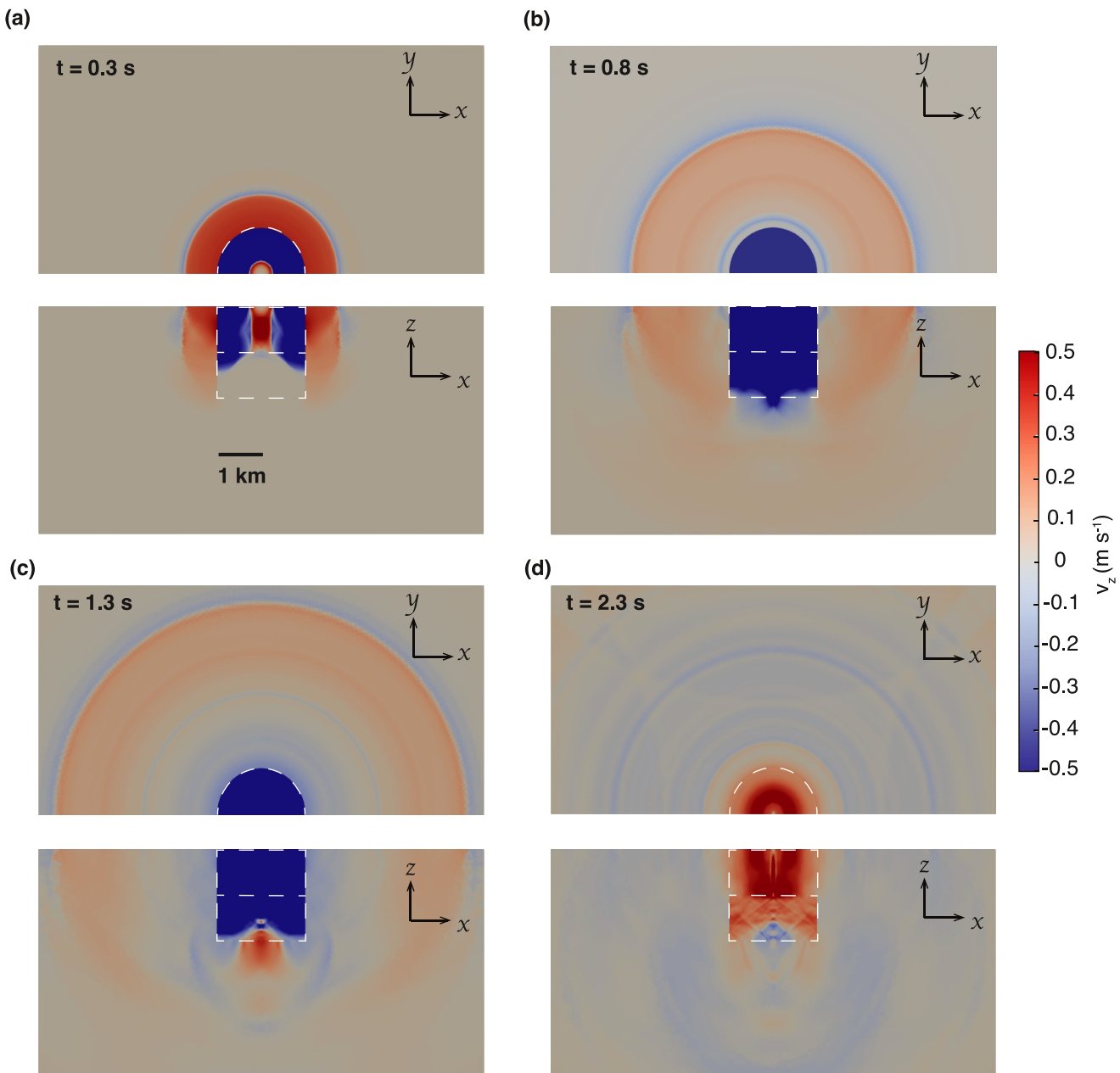


Figure 2. Snapshots of a 3D benchmark case simulation for caldera collapse with basaltic magma (compressible magma with zero viscosity and shear modulus). v_z : vertical particle velocities. (a) Downward axisymmetric collapse of the caldera block sets off elastic rebound outside of the ring fault and downward P-waves in the chamber. (b) Downward collapse of the caldera block continues. (c) Caldera block and magma column decelerate due to chamber pressure increase, resulting in the transmission of downward momentum from the caldera block and magma into the surrounding crust. (d) Cessation of fault slip and subsequent rebound due to elastic strain energy stored in the crust and chamber converting back to kinetic energy.

rates as the magma at the center of the chamber descends faster than that near the chamber walls. Hence $\Delta\sigma_{rz}$ is positive and has highest magnitudes near the walls (downward flow rate decreases in magnitude with increasing radial distance from the axis of the cylindrical chamber, r). This viscous drag effect is completely absent in the basaltic simulation. Additionally, deviatoric stresses transmitted via S-waves are pronounced near the center of the chamber (region 3 in Figure 4a). $\Delta\sigma_{rz}$ is negative here because it is dominated by elastic strain, which is proportional to the gradient of downward displacement (at 1.3 s, downward displacement has the largest magnitude at the chamber walls, since downward magma flow initiates near the ring fault and propagates inward). With this specific simulation, viscous drag force due to boundary layer development is the main mechanism for

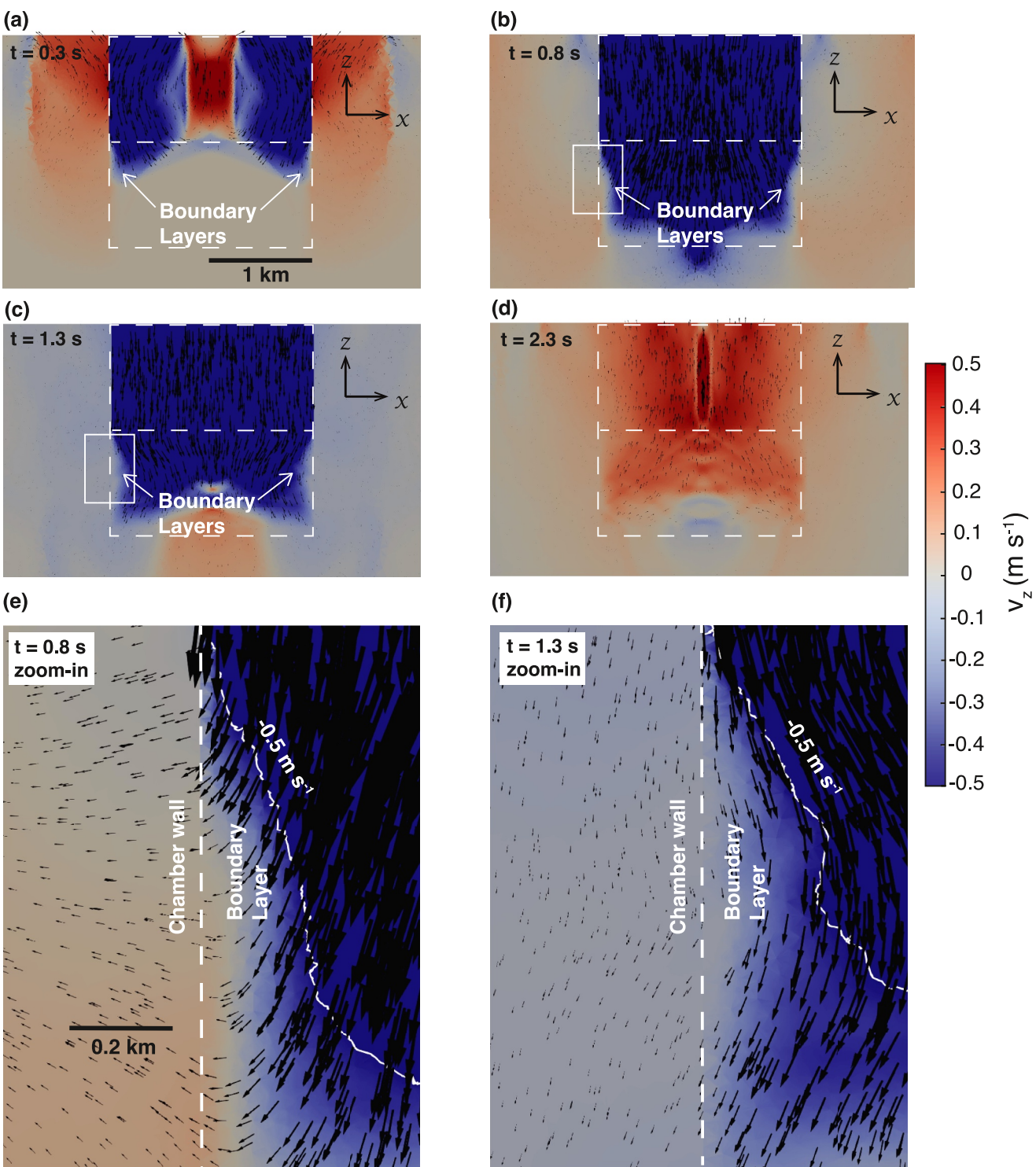


Figure 3. Snapshots of a 3D benchmark case simulation for caldera collapse with silicic magma (linear Maxwell viscoelastic fluid with relaxation in deviatoric stresses). v_z : vertical particle velocities. (a-d) Development of viscous boundary layers along the side walls of the magma chamber. The dynamics in the crust is largely the same as observed in Figure 2. (e, f) Zoomed-in view of the viscous boundary layers, indicated by the region between the chamber wall and the white curve marking $v_z = -0.5$ m s^{-1} (approximately the maximum vertical downward velocity in the chamber). Arrows indicate local flow directions and scale with particle velocity magnitude.

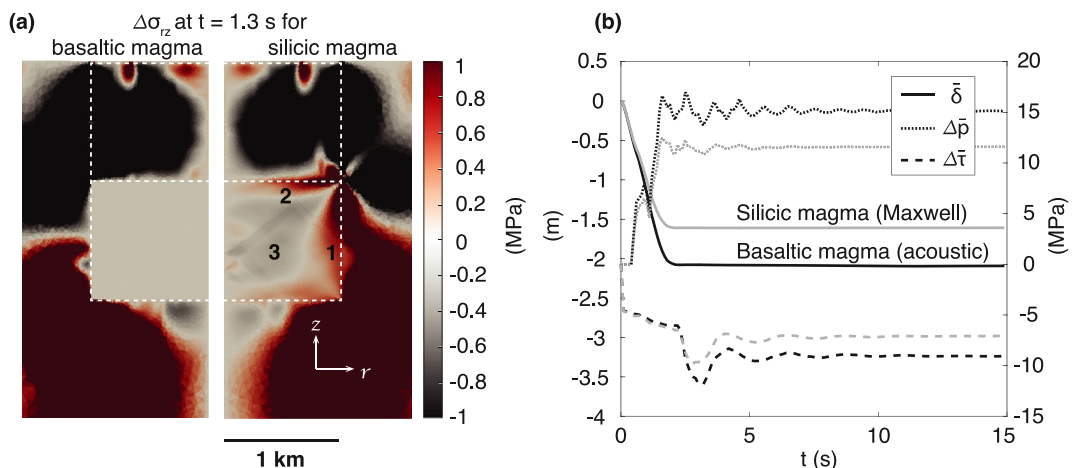


Figure 4. Effect of magma viscosity on collapse dynamics. (a) A snapshot of $\Delta\sigma_{rz}$ at $t = 1.3$ s for basaltic (left) and silicic magma (right). Region 1, 2 denote large magnitude of $\Delta\sigma_{rz}$ due to viscous stresses. Region 3 denotes moderate magnitude of $\Delta\sigma_{rz}$ due to S-waves. (b) Ring fault-averaged slip, $\bar{\delta}$, ring fault-averaged shear stress change, $\bar{\Delta\tau}$, and chamber-averaged pressure change, $\bar{\Delta p}$, as a function of time. The magnitudes of $\bar{\delta}$, $\bar{\Delta p}$, $\bar{\Delta\tau}$ are smaller for silicic magma (modeled as linear Maxwell fluid) than for basaltic magma (modeled as acoustic fluid) due to viscous drag arising from boundary layers shown in (a).

transferring vertical momentum laterally into the crust. In cases where $\tau_M/T_{col} \gg 1$, elastic deviatoric stresses could be the dominant mechanism for laterally transferring vertical momentum into the crust, thereby reducing fault slip.

The viscous drag force on the magma is proportional to the magnitude of downward magma flow velocity, which, in turn, is proportional to the slip rate on the ring fault. Magma viscosity, therefore, acts as a rate-dependent damping mechanism to the ring fault slip rate by transferring the downward momentum of the caldera block laterally into the crust through the chamber walls. The time-integrated effect of this damping mechanism is pronounced in the time history of ring fault-averaged slip, $\bar{\delta}$, ring fault-averaged shear stress change, $\bar{\Delta\tau}$, and chamber-averaged pressure change, $\bar{\Delta p}$ (Figure 4b). For both the basaltic and silicic collapses, $\bar{\Delta\tau}(t)$ decreases to -4.6 MPa initially due to a drop in fault strength, initiating slip on the ring fault. The magnitude of $\bar{\delta}(t)$ continues to increase until it plateaus at $S_{col} = 2$ m at $T_{col} = 2.1$ s. This is because fault slip reduces chamber volume, V , and increases $\bar{\Delta p}$, bringing the caldera block into static force equilibrium in the vertical direction. Between 0 and 2.1 s, $\bar{\Delta\tau}(t)$ decreases slightly due to decrease of ring fault-averaged normal stress. The fault normal stress change, $\bar{\Delta\sigma}$, is induced by ring fault unclamping due to magma chamber pressurization and the resulting elastic deformation of the crust, although the magnitude of the associated strength drop, $f_d\bar{\Delta\sigma}$, is a small contribution to coseismic stress drop, $\bar{\Delta\tau}(t = T_{col})$ (Figure S1 in Supporting Information S1). At 2.1 s, $\bar{\Delta\tau}(t)$ decreases again due to dynamic overshoot, or drop in fault shear stress below the residual strength ($f_d\bar{\sigma}$) due to inertia. After fault slip stops, $\bar{\Delta p}(t)$ exhibits ~ 10 s of transient perturbations due to wave reflections in the chamber. In the basaltic collapse, the stress drop due to dynamic overshoot is of the same magnitude as the initial drop in fault strength. In the silicic collapse, the stress drop due to dynamic overshoot is smaller than the strength drop (Figure 4b). Correspondingly, the final magnitude of $\bar{\Delta p}$ and $\bar{\delta}$, which relate to $\bar{\Delta\tau}$ via the momentum balance (Equation C1), are also smaller in the silicic than in the basaltic collapse. Overall, the viscous drag force in the magma reduces S_{col} by approximately one fourth, but has negligible influence on T_{col} (Figure 4b). Compared to the basaltic collapse, transient pressure perturbations due to P-wave reflections during silicic collapse are more damped (Figure 4b). In addition to viscous damping, wave radiation is also a rate-dependent damping mechanism that can reduce the magnitude of dynamic overshoot. Next we investigate this effect.

3.2. Seismic Wave Radiation Through the Magma Chamber and Ring Fault

During caldera collapse earthquakes, seismic waves radiate out from both the ring fault and the bottom of the caldera block. Because seismic waves carry momentum, they can exert frequency-dependent influence on caldera block motion. We focus on P-wave radiation through the bottom of the caldera block (Figures 2 and 3), because P-

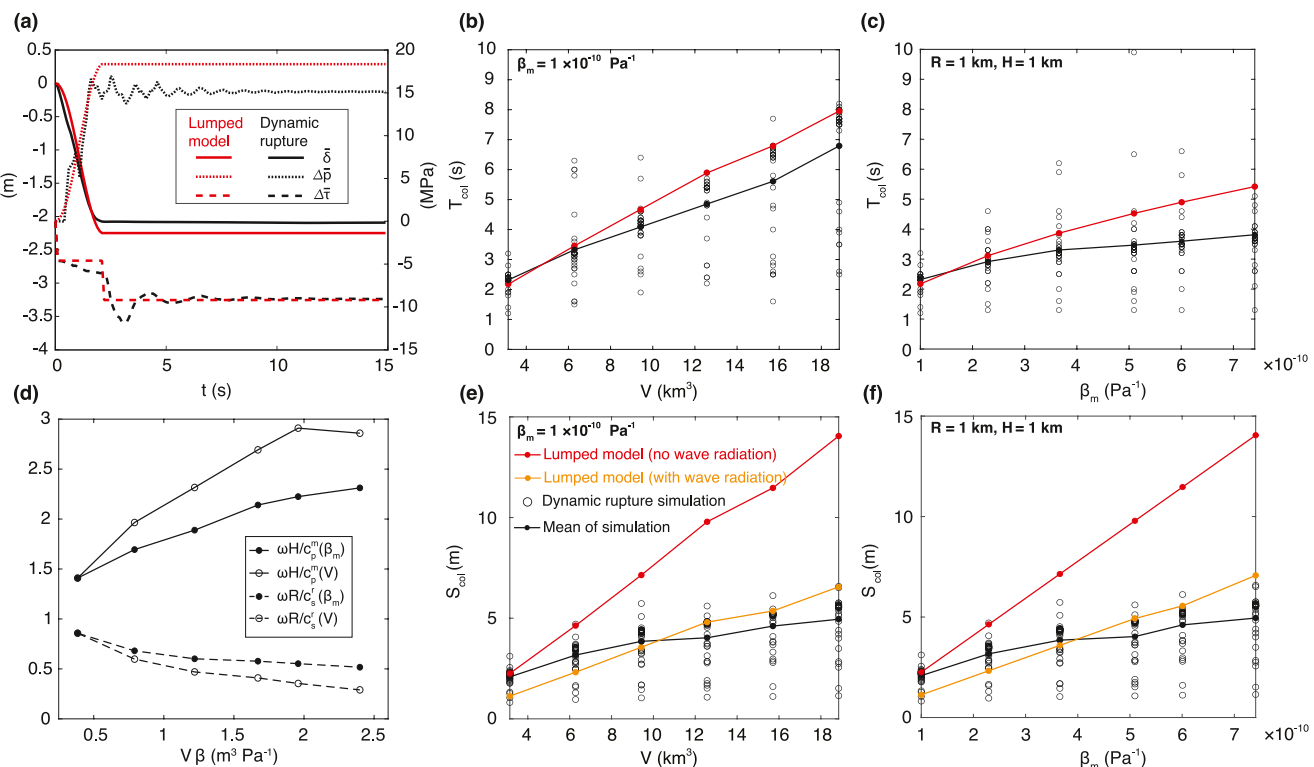


Figure 5. Variation of slip duration and magnitude as a function magma chamber volume and magma compressibility. (a) Time-domain, spatially averaged, numerical solutions of fault slip, $\bar{\delta}$, chamber pressure change, $\Delta\bar{p}$, shear stress change, $\Delta\bar{\tau}$, compared to that of the lumped model, which does not account for wave radiation. (b, c) Duration of the collapse phase (black circles), T_{col} , derived from dynamic rupture simulations and the mean (black solid circle), compared to that of the lumped model (red solid circles). (d) Dimensionless parameters as a function of $V\beta$ (V : chamber volume and total compressibility, respectively). Note that $\beta = \beta_m + \beta_c$, where β_m is magma compressibility. β_c is chamber compressibility, which varies as a function of chamber height and take on the following values 2.3×10^{-11} , 2.6×10^{-11} , 2.9×10^{-11} , 3.3×10^{-11} , 2.5×10^{-11} , 2.7×10^{-11} Pa $^{-1}$ for increasing V . (e, f) Slip magnitude of the collapse phase (black circles), S_{col} , derived from dynamic rupture simulations and the mean (black solid circles), compared to that of the lumped model (red solid circles). Also shown is S_{col} predicted by lumped model accounting for wave radiation (yellow solid circles). Variability of simulation-derived T_{col} , S_{col} arises from the rupture process and depth-dependent elastic response relating slip to shear and normal stress changes on the fault.

waves are the dominant momentum-carrying radiation in the chamber. When the wavelength in magma is long compared to the chamber height, or $\omega H/c_p^m \ll 1$ with c_p^m denoting the P-wave speed in magma, the magma motion decreases linearly with depth. Thus, magma impedes ring fault motion through a spatially uniform pressure increase that applies an upward force on the caldera block in the opposite direction of subsidence. In this limit, the response of the magma is quasi-static and wave effects are negligible, as commonly assumed in lumped models. When the wavelength is short compared to the length scale of the chamber, or $\omega H/c_p^m \gg 1$, only a portion of the total magma volume is affected by wave motion at a given time. In this limit, seismic waves can reduce fault stress drop and slip rate via radiation damping, or the damping of fault motion via seismic wave radiation.

We investigate the effect of wave radiation through the caldera block/magma interface on T_{col} and S_{col} with a set of benchmark simulations with basaltic magma. The simulations are set up such that results can be directly compared to the lumped model of Wang et al. (2022), which does not account for wave effects. All simulations are axisymmetric, with rupture initiated uniformly on the ring fault. An example time domain solution, as well as the corresponding lumped model prediction, is shown for $H = 1$ km and $\beta_m = 1 \times 10^{-10}$ Pa $^{-1}$ (Figure 5a). Because the significance of wave radiation depends on the dimensionless parameter $\omega H/c_p^m$, we perform a parameter sweep with respect to chamber volume V (corresponding to 6 evenly spaced values of H from 1 to 6 km, with $R = 1$ km and $\beta_m = 1 \times 10^{-10}$ Pa $^{-1}$) and magma compressibility β_m (6 values from 1×10^{-10} to 7.4×10^{-10} Pa $^{-1}$, with $H = 1$ km), the latter of which is related to c_p^m via $c_p^m = (\beta_m \rho_m)^{-1/2}$. The range of the parameters is chosen such

that (a) $\omega H/c_p^m$ is larger than unity (ω approximated with $2\pi/T_{col}$), isolating the effect of wave radiation through caldera block/magma interface (Figure 5d) and (b) for each pair of V and β_m (e.g., $V = 3.14 \text{ km}^3$ in Figure 5e and $\beta_m = 1 \times 10^{-10} \text{ Pa}^{-1}$ in Figure 5f), the corresponding $V\beta$ is the same so that S_{col} is expected to be the same based on the lumped model (Equation 4).

For each value of V and β_m , we compare T_{col} , S_{col} derived from numerical solutions with analytical solutions of the lumped model. For numerical simulations, T_{col} at a particular location on the ring fault is determined as the time at which local slip rate drops below $1 \times 10^{-2} \text{ m s}^{-1}$, and S_{col} is determined as the total slip at time T_{col} . T_{col} , S_{col} are sampled along the depths of the ring fault to capture their spatial variability, which arises from the rupture process and depth-dependent elastic response relating slip to shear and normal stress changes on the fault. The lumped model prediction of T_{col} is slightly larger than the mean of numerical solutions at large V and β_m (Figures 5b and 5c), although the discrepancy is small, given the range of numerical solutions (the larger $V\beta$ is, the longer the collapse duration, and the more difficult to numerically determine T_{col} with a threshold slip rate). However, the lumped model overpredicts the mean S_{col} by up to a factor of two at large V and large β_m (Figures 5e and 5f), or large $\omega H/c_p^m$ values (i.e., when wave effects are important; Figure 5d). When a collapse earthquake is damped by seismic wave radiation, dynamic overshoot in $\Delta\bar{\tau}$ is reduced, and up to a factor of two reduction in S_{col} is expected. Therefore, the discrepancy in the lumped model prediction and numerical simulation results for S_{col} is attributed to radiation damping.

For seismic wave radiation through the ring fault (Figures 2 and 3), the relevant waves are S-waves propagating inward and outward from the cylindrical fault. The relevant dimensionless parameter is $\omega R/c_s^r$, with c_s^r denoting S-wave speed in the crust. Due to the high computational cost of dynamic rupture simulations, we did not perform additional simulations with regard to variations in $\omega R/c_s^r$ (although $\omega R/c_s^r$ does vary slightly with ω for the parameter sweep; Figure 5d). Instead, we seek insight by developing Fourier series solutions to the elastic wave equation for an idealized 2D antiplane shear ring fault problem (Appendix B). When the wavelength is long compared to the length scale of the ring fault, R ($\omega R/c_s^r \ll 1$), the displacements within the caldera block are approximately uniform. Thus the block behaves like a rigid mass, as assumed in previous lumped models (Gudmundsson et al., 2016; Kumagai et al., 2001; Roman & Lundgren, 2021; Segall & Anderson, 2021; Wang et al., 2022). Waves and quasi-static deformation (elastic deformation in the absence of inertia) outside of the ring fault contribute minutely to fault slip. When the wavelength is short compared to the length scale of the ring fault ($\omega R/c_s^r \gg 1$), frequency-dependent wave effects are important. In particular, when the shear modulus and/or density of material inside the ring fault are extremely high compared to those outside of the ring fault, the effect of wave radiation on ring fault slip is similar to that for shear slip on planar faults (Geubelle & Breitenfeld, 1997). As we will show next via a lumped model approximately accounting for wave radiation, in the $\omega R/c_s^r \gg 1$ limit, ring fault wave radiation, similar to chamber wave radiation, can reduce S_{col} by up to a factor of two. Additionally, resonance effects could be important when $\omega R/c_s^r$ is slightly larger than unity (Figure B1b). Resonance effects are subdued if slip concentrates on one side of the ring fault (Figure B1e), a scenario relevant for the initiation of caldera collapse earthquakes and trap-door faulting (Amelung et al., 2000; Sandanbata et al., 2022).

We approximate the effects of wave radiation from caldera block/magma interface or ring fault by adding a radiation damping term, $\epsilon A \rho c \dot{\delta}$ (ϵ : a dimensionless factor of order unity encapsulating the importance of wave radiation; $\dot{\delta}$: fault slip rate; ρ , c , A : relevant density, wave speed, and surface area), to the momentum balance of the coupled caldera block and magma chamber system in the lumped model (Appendix C). The value of ϵ can be chosen based on a regime diagram parameterized by $\omega R/c_s^r$ and $\omega H/c_p^m$ (Figure 6a). For example, $\omega H/c_p^m \gg 1$ and/or $\omega R/c_s^r \gg 1$ correspond to $\epsilon \approx 1-2$, otherwise $\epsilon < 1$. As ϵ increases, the slip history computed from the lumped model transitions from being under-damped to over-damped, with the maximum damping reducing S_{col} by half and slightly lengthening T_{col} (Figure 6b). In the benchmark simulations, $\omega H/c_p^m > 1$ and $\omega R/c_s^r < 1$ (Figure 5d). Using $\epsilon \approx 2$, the lumped model accounting for wave radiation nicely explains the reduction in S_{col} as predicted by benchmark simulations (Figures 5e and 5f). However, this approximation of radiation damping neglects resonance effects (Appendix B), and the precise functional form of ϵ cannot be analytically obtained, highlighting the limitations of lumped models in emulating collapse dynamics. Further applications of the regime diagram to historic caldera collapses are discussed in Section 5.1.

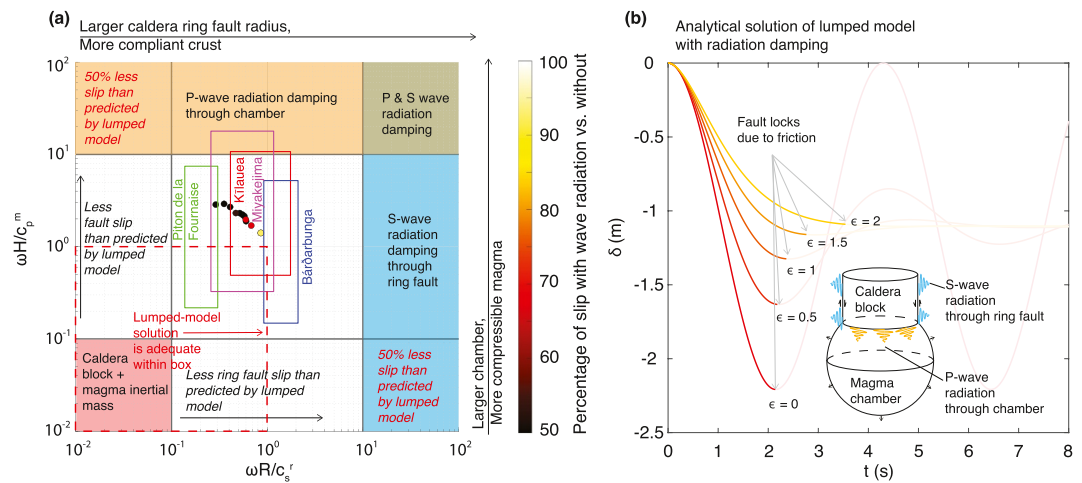


Figure 6. Effect of wave radiation on ring fault slip magnitude. (a) Regime diagram showing the effect of wave radiation on ring fault slip. Red dashed box indicate the region inside of which the lumped model without accounting for wave radiation is adequate for predicting coseismic slip magnitudes. Boxes labeled with volcano names indicate historic caldera collapses and their corresponding location on the regime diagram. (b) Lumped model prediction of ring fault slip, δ , as a function of time, assuming radiation damping of the form $\epsilon A \rho c \dot{\delta}$: ϵ : a factor of order unity encapsulating importance of wave radiation; $\dot{\delta}$: fault slip rate; ρ , c , A : relevant density, wave speed, area. For $\omega H/c_p^n \gg 1$ and/or $\omega R/c_s' \gg 1$, $\epsilon \sim 1-2$, otherwise $\epsilon < 1$.

4. Application to Kīlauea Caldera Collapse in 2018

Here we simulate a caldera collapse earthquake based on observations from Kīlauea volcano in 2018 (Figure 7), accounting for ring fault rupture nucleation, propagation, radiation of seismic waves, and the pressurization of the underlying magma chamber. The objective is to associate each phase of the synthetic waveforms with caldera

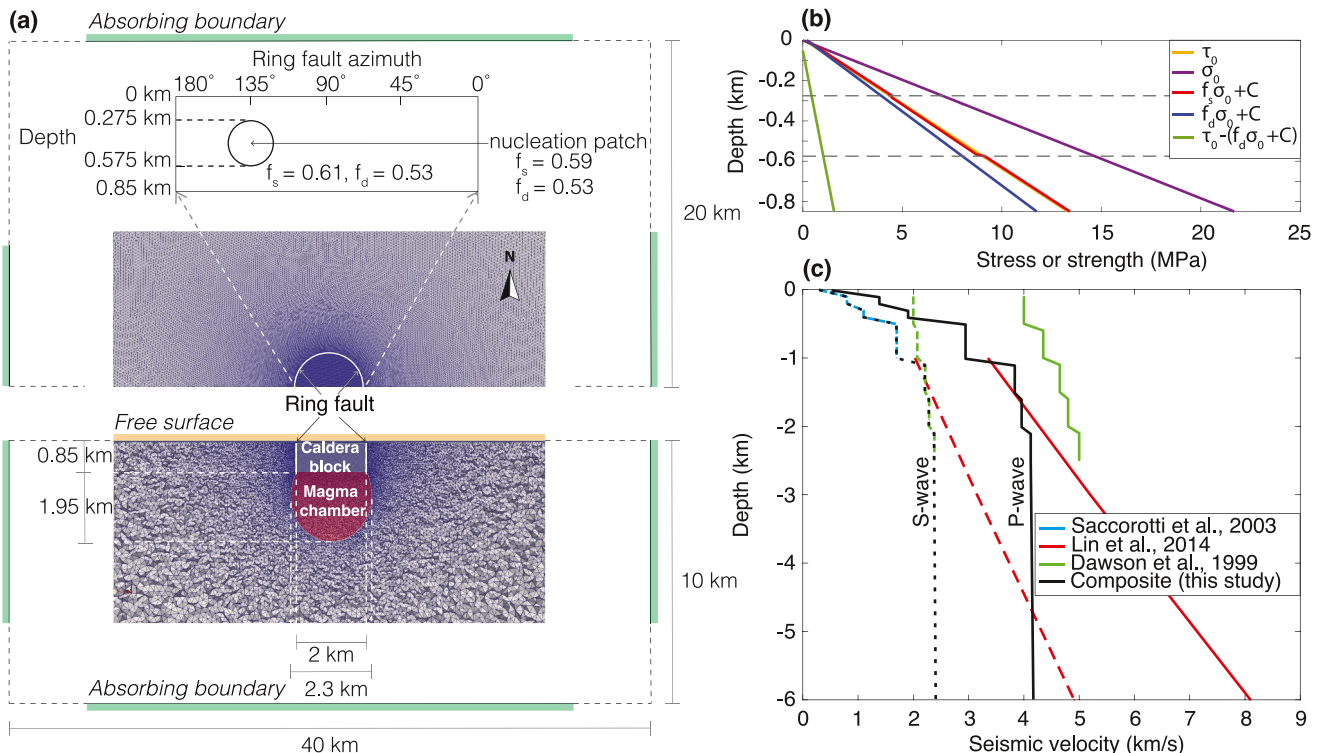


Figure 7. (a) 3D simulation setup for the Kīlauea case showing tetrahedral mesh, boundary conditions, and caldera geometry. Inset shows the location of the circular nucleation patch and frictional coefficients inside/outside of the patch. (b) Initial conditions on fault stress and strength. (c) Composite 1D velocity model used in this study, assuming Poisson ratio of 0.25. τ_0 , σ_0 , f_d , f_s , C : initial shear, normal stresses, and static, dynamic friction coefficients, cohesion.

collapse dynamics, and guide interpretations of observed waveforms. We set up an axisymmetric caldera system (Figure 7a) due to large uncertainties regarding the chamber and ring fault geometries, although complex ring fault geometries involving multiple fault strands or long-wavelength roughness can be incorporated in the simulations. We assume a vertical ring fault, as inferred through modeling of coseismic deformation (Segall et al., 2022). At Kīlauea, a geometrically simple, liquid-dominated, sub-caldera reservoir is supported by isotope geochemistry (Pietruszka & Garcia, 1999) and decades of geodetic modeling of summit deformation, including immediately prior to (K. Anderson et al., 2019) and after (Wang et al., 2021) the 2018 caldera collapse eruptions. We therefore model the reservoir as a spheroidal cavity, filled with basaltic magma idealized as an inviscid, acoustic (compressible) fluid (Table 1). The volume (5.5 km³), shape (prolate spheroid with an aspect ratio of 1.1), and depth to the top of the magma chamber (0.85 km) are approximately based on the median model inverted from pre-caldera collapse deformation (K. Anderson et al., 2019).

In the simulation, fault rupture is artificially nucleated in a circular region with a radius of 150 m and at a depth of 425 m, in the northwest quadrant of the ring fault by reducing the static friction coefficient inside the nucleation region (Figures 7a and 7b; Table 1). The nucleation patch size is carefully selected to be slightly larger than the critical dimension for spontaneous rupture propagation, so as to avoid artificially abrupt rupture nucleation. Due to the axisymmetry of the caldera system, we duplicate receivers in 90° azimuthal intervals with respect to the center of caldera block, such that only one simulation is required to obtain seismic waveforms for earthquakes initiating at various quadrants of the ring fault. The initial normal stress, σ_0 , is assumed to be lithostatic, assuming a constant rock density of 2.7×10^3 kg m⁻³ (Figure 7b). The initial shear stress, τ_0 , is assumed to be a linear function of depth and everywhere 0.1 MPa below the static strength, $f_d\sigma_0 + C$ (C : cohesion), except inside the nucleation patch. Thus, the stress drop, $\tau_0 - (f_d\sigma_0 + C)$, increases as a function of depth. We adopt a composite 1D elastic property model (Figure 7c) with attenuation. The elastic model uses the S-wave velocity model of Sac-
corotti et al. (2003) for depths shallower than 1 km and that of Dawson et al. (1999) for depths between 1 and 2.5 km. The approximate velocity model of Lin et al. (2014) for the Kīlauea region is also shown for reference (Figure 7c). The attenuation model uses a P-wave quality factor, $Q_p = 100$, obtained by approximately averaging the 1D model from Lin et al. (2015) over the appropriate depth range, and a S-wave quality factor, $Q_s = 50$.

4.1. Simulated Rupture Propagation and Collapse

Fault slip initiates at time zero and propagates outwards. Because the stress drop is higher at depth (Figure 7b), the rupture propagates slightly faster downwards than upwards. By 0.2 s, the ring fault rupture has reached the magma chamber, but has not yet reached the surface (Figures 8a and 8b). The fault slip rate is the highest at the edge of the expanding rupture due to high stress concentrations.

By 0.7 s, the ring fault rupture reaches the surface at the northwest of the caldera (Figures 8a and 8b). Waves emanating from the fault enter the magma chamber, where downward propagating P-waves are initiated (S-waves are not sustained due to the inviscid approximation for basaltic magma; Figure 8c). Meanwhile, rupture continues to expand on the ring fault, allowing a large portion of the caldera block to subside. Subsidence on one side of the caldera block results in a slight upward motion at the opposite side, similar to bending of an elastic beam (e.g., at 1.2 and 1.7 s in Figure 8c).

By 2.2 s, the rupture propagation phase around the ring fault completes, leaving the fault slipping everywhere. The convergence of high slip rate fronts manifests as rapid downward motion inward of the ring fault and strong upward ground velocity outside of the ring fault at the southeast (at 2.2 s in Figures 8a and 8c). This initial rupture process is similar to that seen in 2D antiplane shear simulations on circular faults (O'Reilly et al., 2015).

By 2.7 s, the caldera block subsides relatively uniformly, further compressing the magma in the underlying chamber, and gradually decelerates due to the increasing pressure at the bottom of the caldera block. Next we quantitatively interpret synthetic near-field waveforms in terms of collapse dynamics.

4.2. Interpretation of Seismic Wavefield in Terms of Collapse Dynamics

We divide the collapse dynamics into three stages based on interpretations of displacement waveforms, which, due to the low-pass filtering of time-integration, are effectively quasi-static motions in response to equivalent seismic forces and moment. Each stage is identified based on a distinct phase (up/down or radially outward/

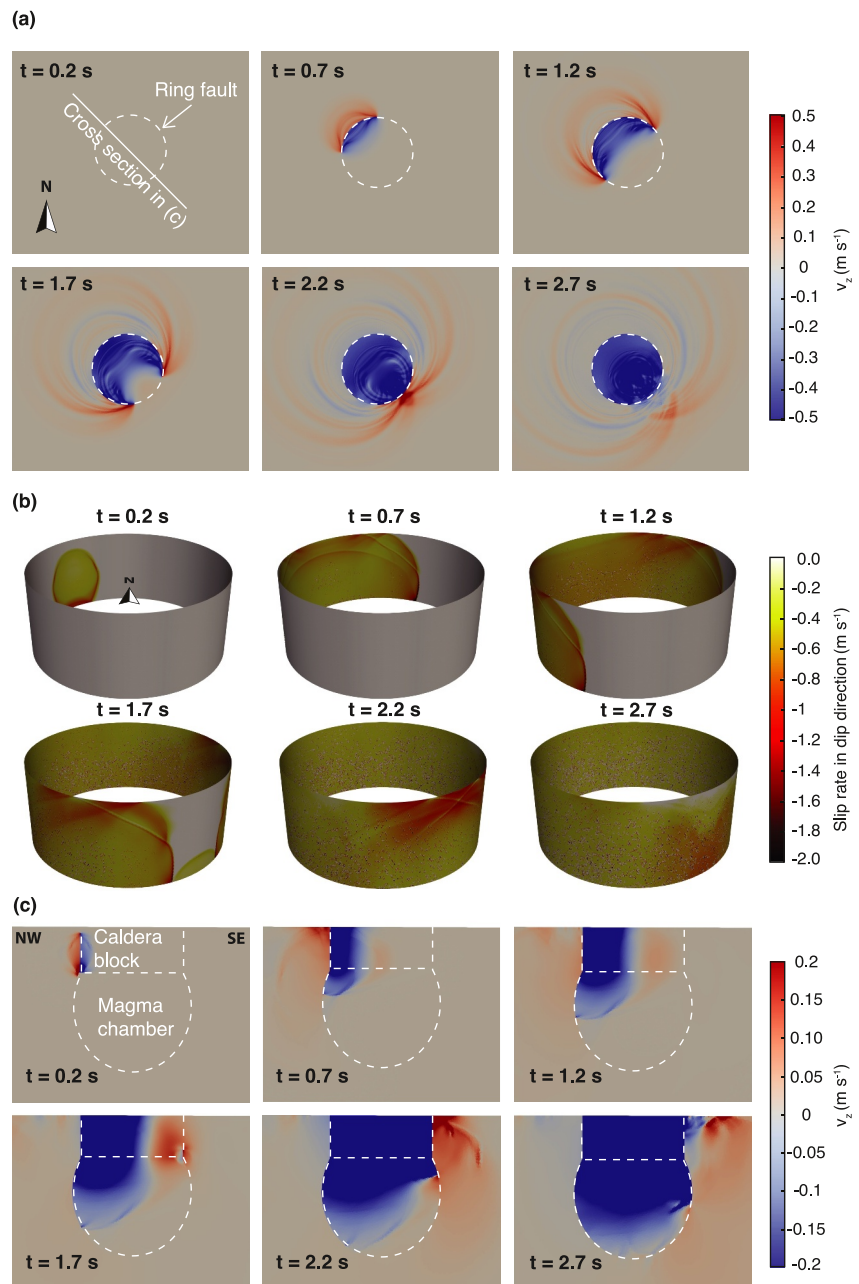


Figure 8. Snapshots of a 3D caldera collapse simulation for Kilauea 2018. For this particular simulation, rupture initiates on the northwest corner of the ring fault, and ends approximately 7 s after rupture initiation, with 1.5 m of total slip. (a) Surface vertical velocity. (b) Slip rate on the ring fault in the dip direction. Negative numbers indicate downward slip. (c) Vertical velocity along the cross section marked in (a).

inward) in the displacement waveforms. The time intervals of various stages are then used for identifying stages in the velocity waveforms.

Stage 1 is characterized by rupture initiation and propagation around the ring fault (Figure 9a). When the rupture initiates, the ring fault motion is dip-slip on a locally planar fault, and motion outside of the ruptured ring fault is that of elastic rebound. The dip-slip motion is a double couple in terms of seismic source representation (Figure 9b). Therefore, near the azimuth of rupture initiation, the tangential (i.e., azimuthal) component of particle velocity is negligible, compared to the radial and vertical components (waveforms at receiver A in Figure 9c). As the rupture expands, the stress concentration at the rupture front grows, resulting in higher slip rates at the rupture

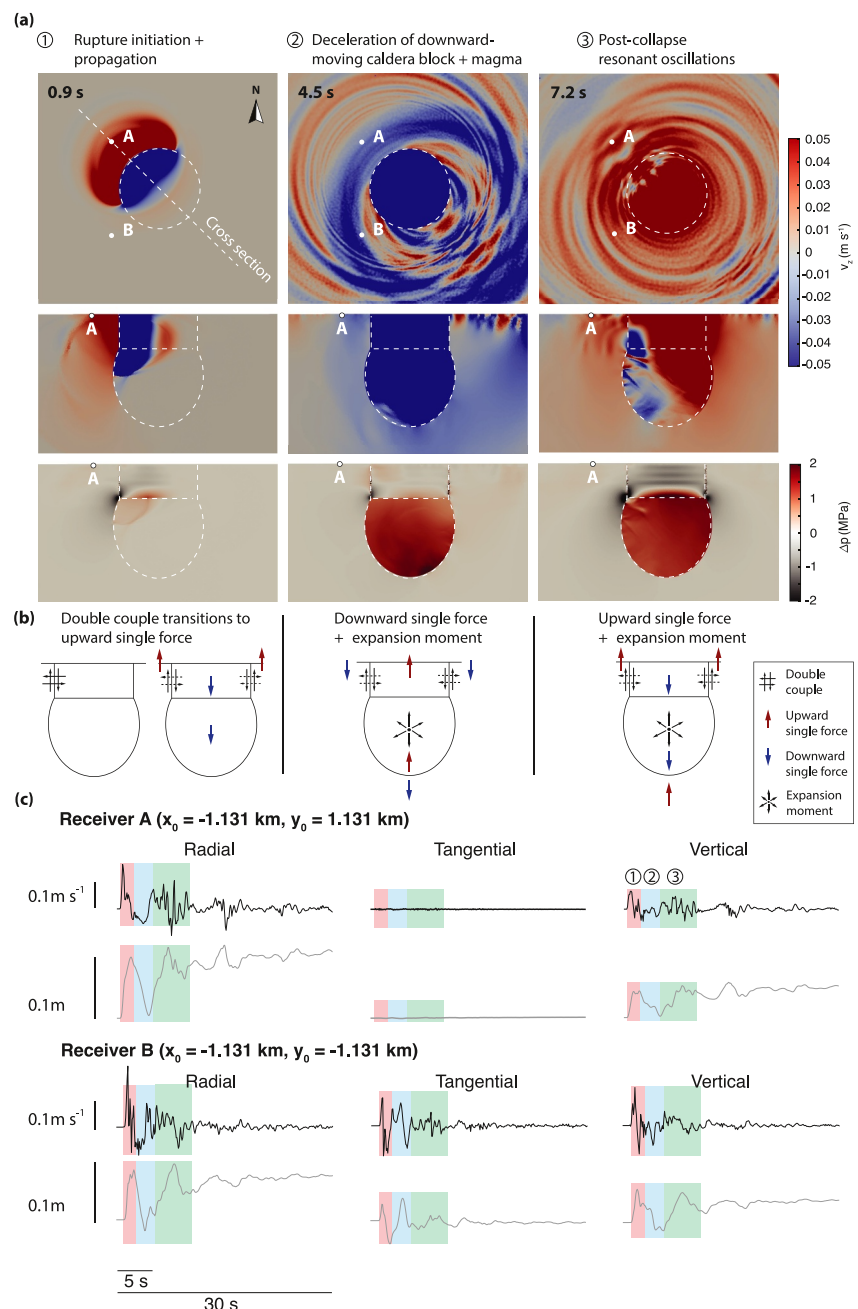


Figure 9. Interpretation of near-field waveforms in terms of collapse dynamics. (a) Vertical velocity in map (first row) and cross section view (second row), with colors saturated to emphasize polarity of ground motion. Pressure change in fluid and mean stress change in solid in cross section view (third row). The wavefield snapshots correspond to three stages of collapse. (b) Seismic representations of collapse stages. (c) Three-component velocity and displacement time series at two locations, A and B, where waveform phases are color-coded in correspondence to collapse stages. Radial and tangential are relative to the surface center of the caldera block.

front and more pronounced directivity effects. This translates to higher amplitude of initial wave arrivals at locations azimuthally farther away from the site of rupture initiation (waveforms at receiver B in Figure 9c). Once the rupture is complete around the ring fault (at 2.2 s in Figure 8), the upward motion outside of the ring fault is more appropriately construed as that due to an upward single force. In terms of mechanics, an upward single force on the crust arises when the caldera block acquires downward momentum (Coppess et al., 2022; Wang et al., 2022). In terms of seismic source representation, the downward force on the caldera block and upward force

on the surrounding crust arise due to cancellation of force couples in the radial directions once the entire fault is slipping (Figure 9b). Because the caldera block is bounded by a free surface above and compressible magma below, the caldera block attains substantial downward momentum over a period of a few seconds. The downward momentum is transferred to the chamber by downward propagating P-waves in the magma, which have yet to reach the bottom of the chamber when the rupture completes around the ring fault (at 2.2 s). Therefore, receivers outside of the ring fault only sense the upward motion due to the upward force (Figure 9c). Associated with the upward force are strong Rayleigh waves, the evanescent character of which is apparent in the exponentially decreasing particle velocity as a function of depth (e.g., the upward velocity at 2.2 s in Figure 8c).

Stage 2 is characterized by the pressurization of the magma chamber, as well as the deceleration of the caldera block and magma column. This stage begins with the arrival of P-waves at the bottom of the chamber (at 2.7 s in Figure 8c), which injects downward momentum into the crust. Shortly after that, P-waves reflected from the bottom of the chamber reach the bottom of the caldera block, causing chamber-wide pressurization (due to chamber volume reduction and associated magma compression). The chamber pressure increase is the highest at the bottom, and smaller in magnitude toward the top of the chamber (Figure 9a). Thus, chamber pressure increase additionally resolves into an upward force on the caldera block and magma column, causing their deceleration. The upward force on the caldera block and magma column is paired with a downward force on the crust (Figure 9b). The chamber pressurization manifests as an expansion moment (Wang et al., 2022), but the downward force dominates the expansion moment in the near-field, resulting in a downward velocity and displacement observable at all receivers (Figure 9c).

Stage 3 is characterized by the end of fault slip (at approximately 7 s) and a broad upward motion (Figure 9a), followed by a downward motion. This upward motion is caused by an upward force on the crust, which is a reaction force to the downward force on the magma and caldera block. The downward force manifests as a higher pressure increase near the top of the chamber and a lower pressure increase at the bottom of the chamber (Figure 9a). This pressure gradient arises due to the conversion of elastic strain energy in the crust and the magma back into kinetic energy. The kinetic energy will eventually be converted into elastic strain energy, and a downward force on the crust will then cause a downward motion on the surface. The upward-downward force cycle repeats with a period of 7 s, which can be viewed as the natural frequency of a harmonic oscillator (Equation C5). The transient oscillations are superposed on an upward and radially outward static displacement due to the pressurization of the chamber. Therefore, the seismic representation for this stage begins with an upward force and an expansion moment (Figure 9b). The amplitude of ground displacement associated with each cycle decreases over time, reflecting energy dissipation to seismic wave radiation. Because there is no net mass loss to the system, the single force eventually returns to zero. The only static displacement remains is that due to chamber pressurization.

We compare simulated velocity waveforms and static displacements with near-field observations at Kilauea for selected collapse earthquakes in July 2018 (when collapses localized to a persistent ring fault structure around the caldera; e.g., K. Anderson and Johanson (2022)). We focus on observations of individual earthquakes, rather than observations stacked over multiple earthquakes (e.g., Segall et al., 2022; Wang et al., 2022), so that temporal variability of earthquake dynamics may be revealed. Due to the complexity of structures underneath the volcano, the 1D elastic property model adopted here is less accurate for modeling waveforms at stations farther away from the caldera. Therefore, we focus on data-simulation comparison at one accelerometer, UWE, which is only a few hundred meters from the caldera rim (Figure 10a). A comparison with all available near-field broadband and accelerometer stations can be found in Figure S2 of the Supporting Information S1. Re-located hypocenters (Shelly & Thelen, 2019) indicate that collapse earthquakes initiate at different azimuths around the ring fault (hypocenter locations in Figure 10a). We group the hypocenters into northwest (NW), southwest (SW), and southeast (SE) quadrants (there are no collapse earthquakes with hypocenters on the northeast in July in the catalog, which is shown in Table S1 of the Supporting Information S1), with the geodetically inverted centroid of the Halema'uma'u reservoir ($19^{\circ}24' 32.4''\text{N}$, $155^{\circ}16' 39.72''\text{W}$; see K. Anderson et al. (2019)) as the origin. We select the waveforms from the last earthquake of each quadrant and compare them with the simulation, which is time-shifted based on alignment of stage 1 phase in observed and simulated displacement waveforms. For the earthquake on July 21 (SW initiation), the vertical component of the simulated velocity waveform at UWE matches reasonably well with observations (Figure 10b). The three stages of collapse previously identified in the synthetic waveform can also be identified in the data. Inward of the caldera ring fault, the simulation predicts a downward coseismic subsidence of 2.06 and 2.01 m at GNSS stations CALS and NPIT, respectively, closely

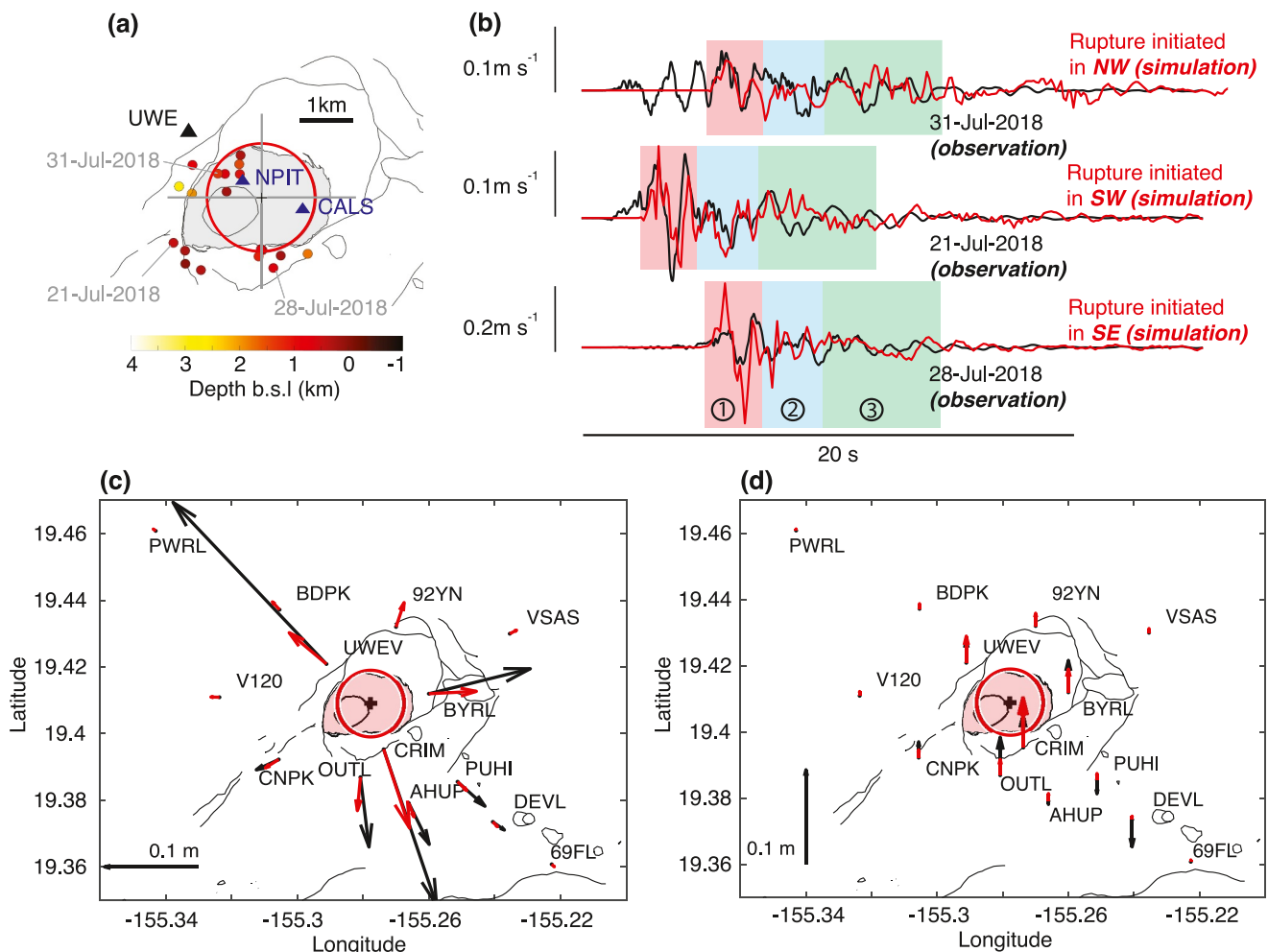


Figure 10. Comparison of observed and simulated ground motions for selected earthquakes at Kīlauea summit in July, 2018. (a) Relocated (VLP) collapse earthquake hypocenters color-coded by depth and grouped into four quadrants. Curves delineate surface topographic features at the caldera. The gray region corresponds to the approximate extent of the ring fault in 2018. Also shown are the location of accelerometer UWE, and intra-caldera GNSS stations NPIT and CALS. (b) Observed and simulated vertical velocity waveforms at accelerometer UWE, corresponding to three earthquakes with hypocenters on the NW, SW, and SE of the caldera. Sections of the waveforms are color-coded by the three stages of collapse (Section 4.2). Simulated velocity waveforms are time-shifted based on alignment of stage 1 phase in observed and simulated displacement waveforms. (c, d) Radial and vertical static coseismic displacements at various extra-caldera GNSS stations (for the earthquake on July 21), compared with simulation. Red circles in (a), (c), (d) show ring fault dimension and location in the simulation.

matching with observed 2.56 m at CALS (the NPIT data is unavailable for this earthquake). Outward of the caldera ring fault, simulated coseismic displacement underpredicts observed radial displacements at stations close to the caldera rim, such as UWEV, CRIM, and BYRL, but reasonably predicts radial and vertical displacements at other stations (Figures 10c and 10d). This is consistent with previous modeling showing that most of the static displacement can be explained by coseismic pressure increase in a vertically oriented, prolate spheroidal chamber, with displacements near the ring fault (in particular, at UWEV) potentially affected by asymmetry in chamber geometry (Segall et al., 2020; Wang et al., 2022). The fit to velocity waveforms is slightly degraded for the earthquake on July 28 (SE initiation), but the three stages can still be identified in the data. The fit to the earthquake on July 31 (NW initiation) is poor. This degradation in fit is attributed to an initial phase in the data that is not present in the simulation, a feature we later identify as a complex nucleation phase of the collapse earthquake (Section 5.2).

In summary, we identify three stages of a caldera collapse earthquake from the simulation and determine their seismic source representations. Stage 1 is the rupture initiation and propagation, which manifests initially as a seismically equivalent double couple, and transitions into an upward single force. Stage 2 is the pressurization of the chamber and the deceleration of the downward moving caldera block and magma, which manifests as an

expansion moment and downward single force. Stage 3 is the post-collapse resonant oscillations, which manifests as a static expansion moment and a transient single force in the vertical direction switching polarities at the natural frequency of the system. Each stage is then identified in observed near-field seismograms at accelerometer UWE during the late stage of the Kilauea caldera collapse of 2018, for collapse earthquakes initiated on the southwest and southeast of the ring fault. For collapse earthquakes initiated on the northwest of the ring fault, an initial phase in the observed waveforms is not captured in the simulation, the implication of which is discussed in Section 5.2.

5. Discussion

5.1. Neglecting Seismic Radiation Overestimates Coseismic Chamber Pressure Increase and Interseismic Duration

Existing models of caldera collapse neglect the effects of seismic wave radiation on collapse dynamics, which is not justified when $\omega R/c_s^r \gg 1$ and/or $\omega H/c_p^m \gg 1$ (Section 3.2). Indeed, the larger the caldera ring fault radius, the larger the chamber, the more compliant the crust, or the more compressible the magma, the less accurate the solutions of coseismic slip and chamber pressure increase become when neglecting radiation damping (Figure 6a). To emphasize this point, we estimate $\omega R/c_s^r$ and $\omega H/c_p^m$ for 4 instrumented basaltic caldera collapses at Miyakejima in 2001, Piton de la Fournaise in 2007, Bárðarbunga in 2014, and Kilauea in 2018, using various constraints available in the published literature (Text S1 in Supporting Information S1). Accounting for large uncertainties in parameters such as chamber dimensions and wave speeds, we find that all 4 caldera collapses potentially overlap with the $\omega R/c_s^r \gg 1$ and/or $\omega H/c_p^m \gg 1$ regime, indicating that radiation damping is crucial for accurately modeling these caldera collapses (Figure 6a).

Neglecting seismic radiation affects models of both individual collapse earthquakes and sequences of earthquakes. For lumped models of individual collapse earthquakes (Gudmundsson et al., 2016; Kumagai et al., 2001; Wang et al., 2022), neglecting radiation damping results in overestimation of coseismic stress drop by up to a factor of two, and correspondingly, overestimation of chamber pressure increase and ring fault slip by up to a factor of two (Figure 6b). For lumped models of earthquake sequences (Roman & Lundgren, 2021; Segall & Anderson, 2021), neglecting radiation damping additionally results in overestimation of interseismic period. To demonstrate this point, we modify the lumped model of Segall and Anderson (2021) to account for ring fault radiation and compare simulation results with and without radiation damping. The Segall and Anderson model considers an axisymmetric caldera block bounded by vertical ring faults, supported below by magma chamber pressure and on the side by shear stress. Magma chamber pressure evolves with collapse induced chamber volume reduction and flank eruption fed by a conduit with constant hydraulic connectivity. Shear stress evolves with rate-and-state velocity-weakening friction. We modify the Segall and Anderson model by adding a term of the form $\epsilon 2\pi RL\rho_r c_s^r \dot{\delta}$ (R : ring fault radius, L : caldera block height, ρ_r : rock density, c_s^r : crustal shear wave speed, $\dot{\delta}$: slip rate), such as in Section 3.2, to the momentum balance equation of the caldera block. We perform two simulations, one with full inertia of the caldera block (without wave radiation, or $\epsilon = 0$), and one with ring fault wave radiation in addition to inertia ($\epsilon = 1$). Simulations that neglect seismic wave radiation lead to an overestimation of coseismic chamber pressure increase (Figure 11a) and coseismic slip (Figure 11b), compared to simulations that include radiation damping, in agreement with those predicted by models of individual collapse earthquakes (Figure 6b). Importantly, neglecting seismic wave radiation leads to an overestimation of interseismic period, the part of the earthquake cycle defined by low slip rate, $\dot{\delta}$, and increasing shear stress, τ (the extreme left portion of the phase portraits in Figure 11c). For caldera collapse earthquakes, interseismic stressing rate on the caldera ring fault is controlled by the rate of chamber depressurization (Roman & Lundgren, 2021; Segall & Anderson, 2021; Wang et al., 2023). For a given interseismic stressing rate, reduced stress drop during coseismic period (the extreme right portion of the phase portraits in Figure 11c) due to radiation damping results in shorter time to reach a threshold stress for earthquake nucleation (the top portion of the phase portraits in Figure 11c).

In summary, lumped models with radiation damping (Appendix C) appropriately tuned to a specific caldera using the proposed regime diagram (Figure 6a) are useful for interpreting near-field seismograms at periods longer than the duration of rupture propagation, inferring ring fault averaged friction, estimating chamber volume/

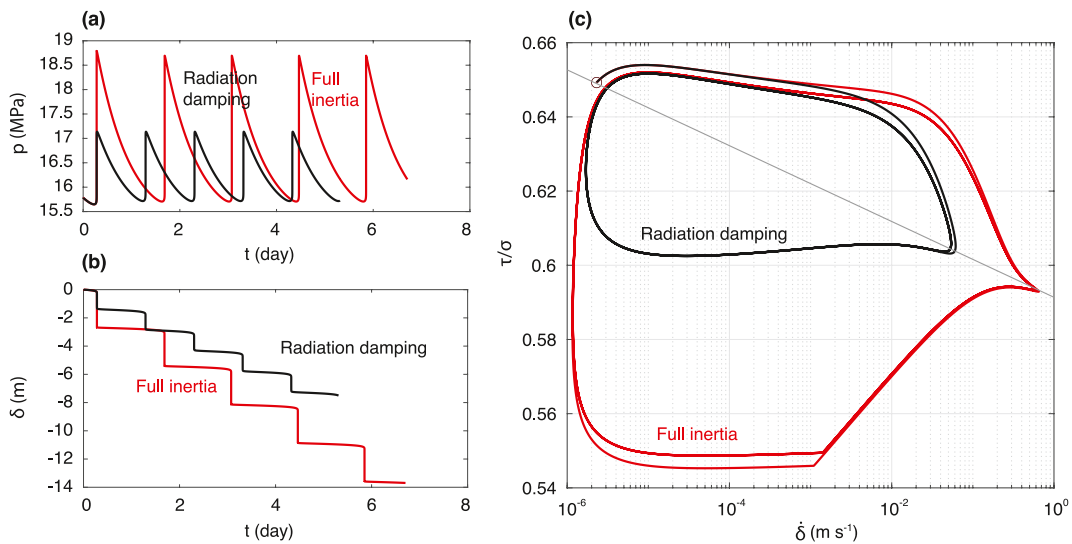


Figure 11. Effect of seismic wave radiation on collapse earthquake sequence. Simulations are done with the lumped model of Segall and Anderson (2021), modified to account for seismic wave radiation from the ring fault. The original model considers an axisymmetric caldera block bounded by a vertical ring fault, supported below by magma chamber pressure and on the side by shear stress. Magma chamber pressure evolves with collapse induced chamber volume reduction and flank eruption fed by a conduit with constant hydraulic connectivity. Shear stress evolves with rate-and-state velocity-weakening friction. (a) Magma chamber pressure, p , over multiple collapse cycles. Pressure surges due to each collapse-induced reduction in chamber volume, and subsequently decreases exponentially due to flank eruption. (b) Cumulative ring fault slip, δ , over multiple collapse cycles. (c) Phase portrait in the fault slip rate ($\dot{\delta}$)—friction coefficient (τ/τ ; τ : ring fault shear stress, normal stress, respectively) space. At a fixed interseismic loading rate, fault stress recovers to a critical level in shorter time when coseismic stress drop is reduced by radiation damping, resulting in a shorter interseismic period.

compressibility, as well as predicting interseismic intervals and ring fault slip magnitudes. However, even though closed-form expressions for radiation damping can be derived for various idealized cases (e.g., axisymmetric, antiplane shear slip on a circular fault, Equation B13), the precise form of radiation damping varies with the geometry of the caldera system. Future studies could use dynamic rupture simulations to establish lumped radiation damping terms as a function of $\omega R/c_s^r$ and $\omega H/c_p^m$, accounting for caldera block and chamber aspect ratios. For questions related to rupture propagation, spatially varied fault friction/stress, and transient magma flows in the underlying chamber, 3D dynamic rupture simulations are required.

5.2. Earthquakes on the Northwest of the Kīlauea Caldera Exhibit Complex Nucleation Phase

We observe that, the simulated velocity waveforms at UWE do not explain the initial phase in the observed waveform for the last earthquake initiated in the NW of the caldera (Figure 10b). Here we seek to understand this unexplained initial phase. We limit the observation period to July 1–July 31 2018, covering the last 22 collapse earthquakes (relocated hypocenters are unavailable for collapse events on July 2 and July 8 2018, therefore excluded from analysis; VLP earthquake catalog in Table S1 of the Supporting Information S1). When grouping the collapse earthquakes by hypocenter location, a consistent pattern emerges: at accelerometer UWE, velocity waveform onset is more emergent and complex for earthquakes initiated in the NW quadrant (except the earthquakes on July 15 and 20), whereas waveform onset is more impulsive for earthquakes initiated in the SW and SE quadrants (Figure 12a). Displacement waveforms (twice integrated from acceleration for accelerometers and once integrated from velocity for broadband seismometers) show a distinct initial phase for earthquakes initiated in the NW that is absent for those initiated in the SW and SE, despite that all three waveforms contain common phases associated with the three stages of collapse (Figure 12b). The presence of this initial phase at stations at a range of azimuths and distances relative to the ring fault suggests that this phase did not arise from path effects (Figure 12c). The absence of this initial phase in simulated

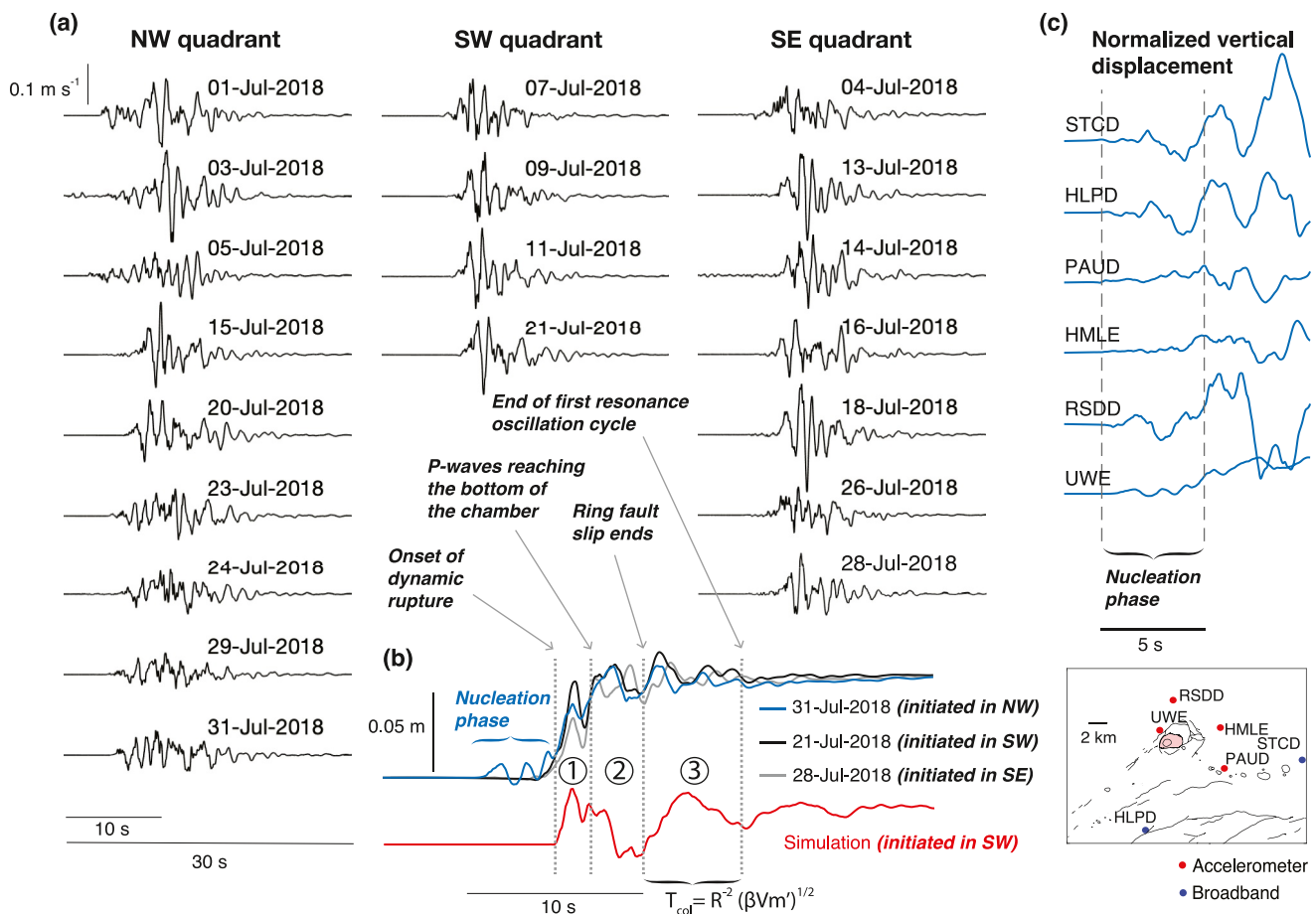


Figure 12. Evidence of complex nucleation phase for earthquakes initiated on the NW section of the ring fault. (a) Three columns show observed, unfiltered, vertical velocity waveforms at accelerometer UWE, categorized by the quadrants in which the collapse (VLP) earthquake hypocenter locates. (b) Simulated vertical displacement waveform is compared to observed waveforms at UWE. Observed waveforms correspond to collapse earthquakes with hypocenters in the NW, SW, and SE quadrants. The simulated waveform is time-shifted based on alignment of stage 1 phase in observed and simulated displacement waveforms. Various stages of collapse (Section 4.2) are identified in both synthetic and observed waveforms at UWE. (c) Zoomed-in view of vertical displacement onset for the July 31 earthquake at various stations (see map in lower right), showing the presence of a nucleation phase at all available near-field stations. Vertical dashed lines demarcate the onset of the nucleation phase and its transition to dynamic rupture. Waveforms are normalized by displacement magnitude 5 s after onset (where the dashed line on the right intersects the waveforms).

displacement waveforms suggests that this phase is associated with source complexities not captured in the simulation.

The irregular shape and low amplitude of this initial phase, followed by a rapid ramp up in displacement, are characteristic of earthquake nucleation phases (Ellsworth & Beroza, 1995). On tectonic faults, the nucleation phase is interpreted in terms of two conceptual models, the cascade model and the pre-slip model (Ellsworth & Beroza, 1995), or a mixture of both on rough faults (Cattania & Segall, 2021). In the cascade model, a large earthquake occurs when a small earthquake triggers a cascade of increasingly large-slip earthquakes. In the pre-slip model, earthquake occurs when an aseismically slipping fault patch grows beyond a critical size. We can not rule out either interpretation for earthquakes initiated on the NW without quantitative comparisons between the initial moment rate history of the VLP collapse earthquakes and closely located $M_w = 2.4 - 4.2$ volcano tectonic (VT) earthquakes in between collapse earthquakes (Shelly & Thelen, 2019). However, we note that, models that invoke smaller earthquakes breaking out to become large collapse earthquakes are potentially more favorable, as it has been shown that the seismically observed onset of a collapse (VLP) earthquake in the SE is similar to that of a much smaller magnitude, but closely located, VT earthquake (Segall et al., 2024). Other observations, such as the gap in the frequency-magnitude distribution between large VT earthquakes and VLP earthquakes, as well as increasing magnitudes of VT earthquakes leading toward the VLP earthquakes, also

support this interpretation (Segall et al., 2024). The fact that the nucleation phase is the most distinct for earthquakes initiated on the NW of caldera indicates strong fault heterogeneity at that location. This heterogeneity may reflect underlying variability in velocity strengthening/weakening friction, as suggested by the simultaneous occurrence of meter-per-day interseismic creep and episodic collapse earthquakes (Wang et al., 2023), or variability in fault roughness.

6. Conclusions

We present the first 3D dynamic rupture simulation for basaltic caldera collapse, building on the open-source software, SeisSol, with extended capability of simulating collapse with silicic magma. The model captures dynamically coupled ring fault rupture initiation and propagation, caldera block subsidence, chamber pressurization, as well as seismic waves in both the solid crust and magma. We perform simulations to (a) understand controls on the duration and magnitude of caldera collapse earthquakes, and (b) guide interpretations of near-field seismic waveforms in terms of collapse dynamics. We find that seismic wave radiation at both the ring fault and the caldera block/magma interface reduce the coseismic ring fault slip magnitude by up to a factor of two, while having negligible effects on slip duration. Seismic radiation is particularly important for calderas with large ring fault radii, large chamber volume, highly compliant crust, or highly compressible magma. To guide future modeling and data interpretation studies, we developed a regime diagram quantifying the importance of radiation damping, based on both simulations and theoretical derivations. We also find that, similar to slip rate dependent damping due to seismic wave radiation, magma viscosity appropriate for silicic magmas reduces caldera collapse magnitude significantly. We specialize the simulation for the 2018 caldera collapse of the Kilauea volcano. A comparison between synthetic and observed near-field seismic waveforms reveals that, the full sequence of collapse earthquake dynamics, from nucleation, rupture propagation, to the end of ring fault slip, as well as magma chamber dynamics, from deceleration of the downward-moving magma column, chamber pressurization, to the resonant oscillations after ring fault slip ends, are well reflected in unfiltered near-field waveforms. Dynamic rupture simulations reveal unprecedented details of caldera collapse mechanics and allow for quantitative interpretations of near-field seismic data in terms of the dynamics. Future studies of caldera collapse earthquakes may utilize these simulations to further establish quantitative relationships between seismic, geodetic, observations and conceptual models of caldera collapse dynamics.

Appendix A: Modeling Silicic Magma With Maxwell Rheology

Here we present a method to approximate the constitutive equations for a homogeneous, isotropic, Maxwell material with relaxation in deviatoric stresses, using the built-in seismic wave attenuation feature of SeisSol.

First we derive the target constitutive equations. For linear viscoelastic materials in general, the stress tensor, σ_{ij} , depends on the history of the strain tensor, ϵ_{ij} (Christensen, 2012; Uphoff, 2020):

$$\sigma_{ij}(t) = G_{ijkl}^c * \dot{\epsilon}_{kl}, \quad (A1)$$

where $*$ denotes convolution and over-dot indicates time derivative. G_{ijkl}^c is the short hand notation for $G_{ijkl}(t)H(t)$, where $G_{ijkl}(t)$ is a fourth order tensor that can be decomposed, assuming isotropic material response, into a bulk relaxation function, $G_1(t)$, and a deviatoric relaxation function, $G_2(t)$ (Christensen, 2012; Uphoff, 2020):

$$G_{ijkl}(t) = \frac{1}{3}(G_2(t) - G_1(t))\delta_{ij}\delta_{kl} + \frac{1}{2}G_1(t)(\delta_{ik}\delta_{jl} + \delta_{il}\delta_{jk}), \quad (A2)$$

where δ_{ij} denotes the Kronecker delta.

To obtain $G_1(t)$ and $G_2(t)$ for a Maxwell material with relaxation only in deviatoric stresses, we first decompose σ_{ij} as the summation of the mean stress, $\sigma_{kk}/3$, and the deviatoric stress tensor, σ'_{ij} :

$$\sigma_{ij} = \sigma'_{ij} + \frac{1}{3}\sigma_{kk}\delta_{ij}, \quad (A3)$$

where repeated indices indicate summation. A similar decomposition is performed on the strain rate tensor, $\dot{\epsilon}_{ij}$ into the dilation rate, $\dot{\epsilon}_{kk}/3$, and deviatoric strain rate, $\dot{\epsilon}_{ij}$:

$$\dot{\epsilon}_{ij} = \dot{\epsilon}_{ij} + \frac{1}{3}\dot{\epsilon}_{kk}\delta_{ij}. \quad (\text{A4})$$

The elastic deviatoric strain rate, $\dot{\epsilon}_{ij}^e$ and viscous deviatoric strain rate, $\dot{\epsilon}_{ij}^v$, are additive, so σ'_{ij} satisfies:

$$\begin{aligned} \dot{\epsilon}_{ij} &= \dot{\epsilon}_{ij}^v + \dot{\epsilon}_{ij}^e \\ &= \frac{\sigma'_{ij}}{2\eta_m} + \frac{\dot{\sigma}'_{ij}}{2\mu_m}, \end{aligned} \quad (\text{A5})$$

where μ_m and η_m are the magma shear modulus and shear viscosity, respectively. In the rest of this section all quantities are associated with magma and we omit the subscript “*m*.” Similarly, the elastic dilation rate, $\dot{\epsilon}_{kk}^e/3$, and viscous dilation rate, $\dot{\epsilon}_{kk}^v/3$, are additive, so σ_{kk} satisfies:

$$\begin{aligned} \dot{\epsilon}_{kk} &= \dot{\epsilon}_{kk}^v + \dot{\epsilon}_{kk}^e \\ &= \frac{\sigma_{kk}}{3\xi} + \frac{\dot{\sigma}_{kk}}{3K}, \end{aligned} \quad (\text{A6})$$

where K and ξ are the magma bulk modulus and bulk viscosity, respectively.

Solving Equations A5 and A6, we obtain

$$\sigma'_{ij} = 2\mu e^{-\frac{\mu t}{\eta}} H(t) * \dot{\epsilon}_{kk}, \quad (\text{A7a})$$

$$\sigma_{kk} = 3K e^{-\frac{Kt}{\xi}} H(t) * \dot{\epsilon}_{kk}. \quad (\text{A7b})$$

We assume that there is no mean stress relaxation, so σ_{kk} is not history-dependent:

$$\sigma_{kk}/3 = K\dot{\epsilon}_{kk} = -p, \quad (\text{A8})$$

where p is the mechanical pressure. Therefore, the target relaxation functions for a Maxwell material are of the following form:

$$G_1^M(t) = 2\mu e^{-\frac{\mu t}{\eta}}, \quad (\text{A9a})$$

$$G_2^M(t) = 3K. \quad (\text{A9b})$$

Equations A9a and A9b is what we ideally seek to solve numerically. Unfortunately, this cannot be done using the current implementation of viscoelastic attenuation in SeisSol. Next we show how Equations A9a and A9b can be approximated using the attenuation feature of SeisSol.

SeisSol uses a Generalized Maxwell Body (GMB) to approximate $G_1(t)$ and $G_2(t)$ of arbitrary forms. For a GMB of N Maxwell bodies, the relaxation functions are of the following form:

$$\nu = 1, 2 : G_\nu^c(t) = \left(Y_{0\nu} + \sum_{n=1}^N Y_{n\nu} e^{-\omega_{n\nu} t} \right) H(t), \quad (\text{A10})$$

where $\omega_{n\nu} = Y_{n\nu}/\eta_{n\nu}$ is the reciprocal of the Maxwell relaxation time.

Combining Equations A1, A2, and A10 yields the stress-strain relationship for a GMB:

$$\begin{aligned}
 \sigma_{ij} &= \frac{1}{3}(G_2^c - G_1^c)\delta_{ij} * \dot{\epsilon}_{kk} + G_1^c * \dot{\epsilon}_{ij} \\
 &= \frac{1}{3}G_2^c \delta_{ij} * \dot{\epsilon}_{kk} + G_1^c * \left(\dot{\epsilon}_{ij} - \frac{1}{3}\delta_{ij}\dot{\epsilon}_{kk} \right) \\
 &= \frac{1}{3}G_2^c \delta_{ij} * \dot{\epsilon}_{kk} + G_1^c * \dot{\epsilon}_{ij} \\
 &= \frac{1}{3} \left(Y_{02} + \sum_{n=1}^N Y_{n2} e^{-\omega_{n2}t} \right) H(t) \delta_{ij} * \dot{\epsilon}_{kk} + \left(Y_{01} + \sum_{n=1}^N Y_{n1} e^{-\omega_{n1}t} \right) H(t) \delta_{ij} * \dot{\epsilon}_{ij}.
 \end{aligned} \tag{A11}$$

At this point, to obtain Equations A9a and A9b exactly, we simply set $N = 1$, $Y_{01} = 0$, $Y_{11} = 2\mu$, $\omega_{11} = \mu/\eta$, $Y_{02} = 3K$, $Y_{12} = 0$, and $\omega_{12} = 0$. However, a major hurdle is that SeisSol utilizes the same set of ω_{nv} for the bulk ($\nu = 2$) and deviatoric relaxation functions ($\nu = 1$). This implementation reduces memory requirements for

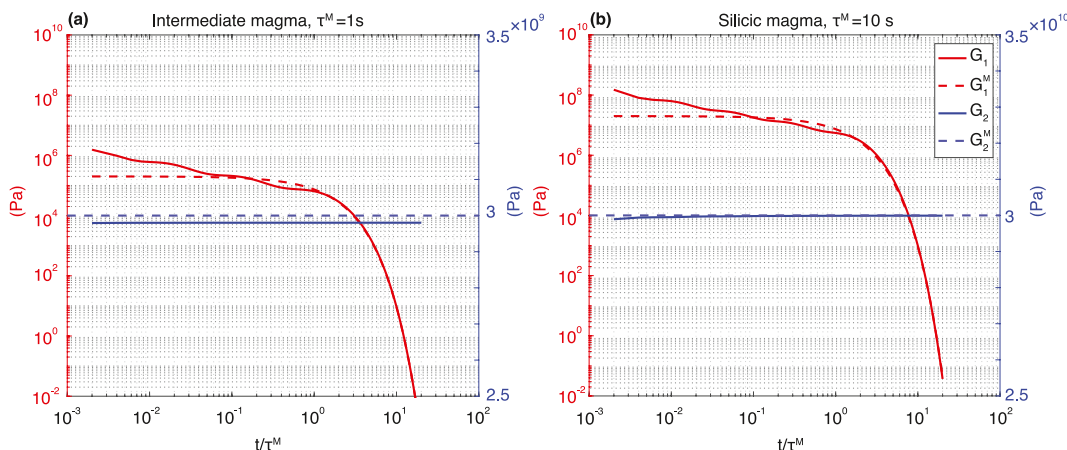


Figure A1. Example target relaxation functions for Maxwell materials, G_1^M , G_2^M , and corresponding SeisSol approximations, G_1 , G_2 , using 9 Maxwell bodies. (a) Magma of intermediate silicic composition with large amount of exsolved volatiles. The target relaxation functions are specified with the parameters: $\mu = 10^5$ Pa, $\eta = 10^5$ Pa s, $\rho = 2.2 \times 10^3$ kg m $^{-3}$, $K = 10^9$ Pa. (b) Magma of high silicic composition with small amount of exsolved volatiles. The target relaxation functions are specified with the parameters: $\mu = 10^7$ Pa, $\eta = 10^8$ Pa s, $\rho = 2.7 \times 10^3$ kg m $^{-3}$, $K = 10^{10}$ Pa. $\tau^M = \eta/\mu$: target Maxwell relaxation time.

computation, but constrains the accuracy of the approximation.

Therefore, to approximate Equations A9a and A9b, we optimize for Y_{01} , Y_{02} , Y_{n1} , Y_{n2} , ω_{n1} , and ω_{n2} such that the following sum of L_2 norm of residual is minimized:

$$L2 = \left\| \left(Y_{01} + \sum_{n=1}^N Y_{n1} e^{-\omega_{n1}t} \right) - 2\mu e^{-\frac{\mu t}{\eta}} \right\|_2 + \left\| \left(Y_{02} + \sum_{n=1}^N Y_{n2} e^{-\omega_{n2}t} \right) - 3K \right\|_2. \tag{A12}$$

The inversion code is provided. In practice, the desired relaxation functions cannot always be approximated well using the GMB, due to a couple of constraints. First, due to implementation considerations in SeisSol, ω_{nv} are required to be evenly spaced in log space and Y_{01} , Y_{02} , Y_{n1} , Y_{n2} are non-trivially interdependent. Second, although increasing the number of mechanisms theoretically increases the ability of GMB to approximate any relaxation function, the larger the number of mechanisms, the higher the computation cost. Thus, we limit our approximation to 9 mechanisms, which reasonably approximate the rheology of typical intermediate and silicic magmas (Figure A1).

Appendix B: Seismic Wave Radiation Through Ring Fault

We investigate the effect of ring fault seismic wave radiation on caldera collapse dynamics through frequency domain solutions for slip on a circular ring fault (Figure B1a). We restrict attention to the 2D antiplane shear problem and thus neglect variations with depth. Elastic properties are allowed to differ inside and outside of the ring fault. The analysis focuses on the relationship between impedance, \hat{Z} (defined as the ratio of ring fault stress change and slip rate in frequency domain), and the dimensionless parameters, $\omega R/c_s^-$, μ^-/μ^+ , ρ^-/ρ^+ . $\omega = 2\pi f$ is the angular frequency, c_s the crustal S-wave speed (superscript r is dropped from now on for simplicity), R the ring fault radius, μ the shear modulus, and ρ the crustal density. “-” and “+” signs denote inside and outside of the ring fault, respectively.

For axisymmetric fault slip (uniform slip rate at all azimuths of the ring fault), we find that, when $\omega R/c_s^- \ll 1$, \hat{Z} takes the form of caldera block inertia (caldera block is effectively rigid and its response dependent only on the block's acceleration and its total mass); quasi-static deformation and wave radiation outside of the ring fault has negligible influence on fault slip (Figure B1b). When $\omega R/c_s^- \gg 1$, \hat{Z} takes the form of radiation damping on planar faults, modulated by troughs corresponding to resonance frequencies. Resonance effects are particularly strong when the shear modulus inside of the ring fault is low compared to that outside of the ring fault (Figure B1b inset). For asymmetric fault slip (slip concentrates on one side of the ring fault), a scenario relevant to trap-door faulting at certain calderas (Amelung et al., 2000; Sandanbata et al., 2022) and the initiation of caldera collapse earthquakes, we show that, when $\omega R/c_s^- \ll 1$, \hat{Z} is influenced by quasi-static deformation of the caldera block (Figure B1c), in addition to inertia. When $\omega R/c_s^- \gg 1$, \hat{Z} can be approximated with radiation damping on planar faults. Asymptotic approximations of \hat{Z} in the $\omega R/c_s^- \ll 1$ limit, as well as radiation damping approximation in the $\omega R/c_s^- \gg 1$ limit, may be combined to derive a lumped parameter model for caldera trap-door faulting (Figure B1e).

We assume an isotropic, linear elastic full space, and consider the 2D antiplane shear problem of slip on a ring fault that is infinite and invariant in the z direction (Figure B1a). Conservation of momentum and linear elasticity yield the cylindrical coordinates scalar wave equation for displacement in z direction, $w(t, r, \theta)$:

$$\frac{1}{c_s^2} \frac{\partial^2 w}{\partial t^2} = \frac{\partial^2 w}{\partial r^2} + \frac{1}{r} \frac{\partial w}{\partial r} + \frac{1}{r^2} \frac{\partial^2 w}{\partial \theta^2}, \quad (B1)$$

where c_s takes the form of c_s^- inside of the ring fault and c_s^+ outside of the ring fault. Next we Fourier transform Equation B1 in time, t , adopting the following convention for Fourier transform and its inverse transform,

$$\mathcal{F}(f(t)) = \int_{-\infty}^{\infty} f(t) e^{i\omega t} dt, \quad (B2a)$$

$$\mathcal{F}^{-1}(\hat{f}(\omega)) = \int_{-\infty}^{\infty} \hat{f}(\omega) e^{-i\omega t} d\omega, \quad (B2b)$$

respectively. We then seek Fourier series solutions in azimuthal angle, θ

$$\frac{\partial^2 \hat{w}}{\partial r^2} + \frac{1}{r} \frac{\partial \hat{w}}{\partial r} + \left(-\frac{n^2}{r^2} + \frac{\omega^2}{c_s^2} \right) \hat{w} = 0, \quad (B3)$$

where n is the dimensionless azimuthal order in θ . To satisfy the periodic boundary condition, $w(\theta = 0) = w(\theta = 2\pi)$, n must be non-negative integers: $n = \{0, 1, 2, \dots\}$.

Equation B3 is the transformed Bessel's equation (Bowman, 2012), with general solutions of the form:

$$\hat{w} = \sum_{n=1}^{\infty} \hat{w}_n e^{i2\pi n\theta}, \quad (B4)$$

where,

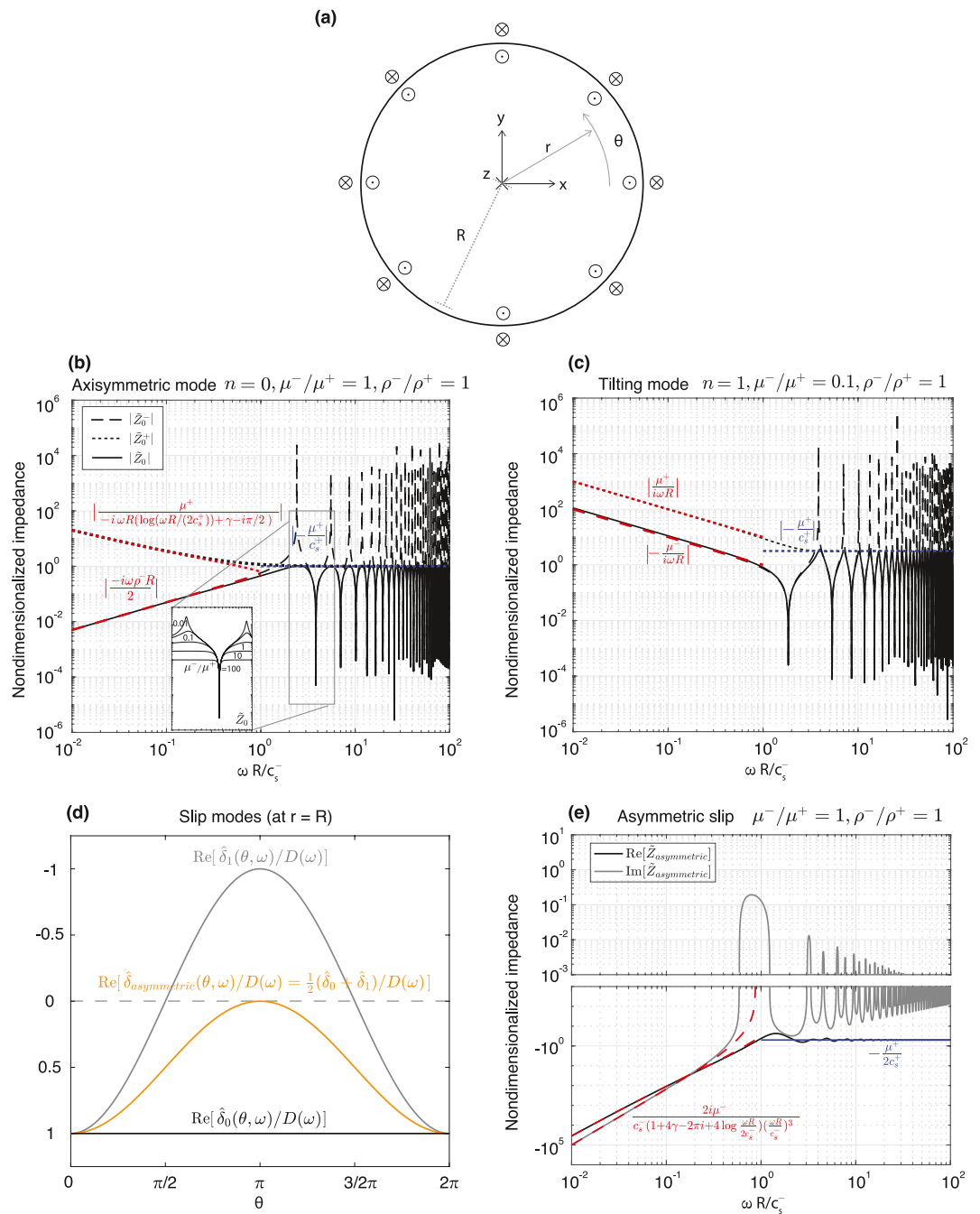


Figure B1. Effect of shear wave radiation on caldera collapse dynamics, in terms of Fourier-domain impedance to ring fault slip. (a) Schematic of the 2D antiplane shear ring fault slip problem. r : radial distance; θ : azimuthal angle; R : ring fault radius. Note elastic properties (μ, ρ) inside and outside of the ring fault can be different. (b) Nondimensionalized impedance for the axisymmetric mode, \tilde{Z}_0 , for $\mu^-/\mu^+ = 1$ and $\rho^-/\rho^+ = 1$. Inset shows \tilde{Z}_0 at $\rho^-/\rho^+ = 1$ and μ^-/μ^+ between 10^{-2} and 10^2 . (c) Nondimensionalized impedance for the tilting mode, \tilde{Z}_1 , for $\mu^-/\mu^+ = 0.1$, $\rho^-/\rho^+ = 1$. (d) Schematic illustrating building asymmetric slip, $\hat{\delta}_{\text{asymmetric}}(\theta, \omega)$, with $n = 0$ mode (axisymmetric mode) and $n = 1$ mode (tilting mode). $\hat{\delta}_n(\theta, \omega)$: fault slip Fourier-transformed in time associated with azimuthal mode, n , and at angular frequency, ω . Note the slip is normalized by the frequency dependent slip amplitude, $D(\omega)$. (e) Real and complex components of the nondimensionalized impedance for asymmetric ring fault slip, $\tilde{Z}_{\text{asymmetric}}$, illustrating the possibility of building a lumped model for trap-door faulting. Note asymptotic limits are labeled in dimensional forms for ease of recognition.

J_n and Y_n denote Bessel functions of the first and the second kind (of order n), respectively, representing standing waves. C_n^1 and C_n^2 are arbitrary constants associated with each order. Because $\lim_{x \rightarrow 0} Y_n(x)$ is unbounded, the general solution for displacement inside of the ring fault, \hat{w}_n^- is:

$$\hat{w}_n^- = C_n^1 J_n\left(\frac{\omega r}{c_s}\right) + C_n^2 Y_n\left(\frac{\omega r}{c_s}\right). \quad (\text{B6})$$

To seek the general solution for displacement outside of the ring fault, we re-write Equation B5 in terms of the Hankel function of the first kind, $H_n^{(1)}$, a linear combination of J_n and Y_n that represents outward traveling waves:

$$\hat{w}_n = C_n^3 J_n\left(\frac{\omega r}{c_s}\right) + C_n^2 H_n^{(1)}\left(\frac{\omega r}{c_s}\right), \quad (\text{B7a})$$

$$C_n^3 = C_n^1 + iC_n^2 \quad (\text{B7b})$$

Because of the infinite domain assumption, the only valid solution outside of the ring fault is that of outward traveling waves:

$$\hat{w}_n^+ = C_n^2 H_n^{(1)}\left(\frac{\omega r}{c_s^+}\right). \quad (\text{B8})$$

For the Fourier series solution, the only relevant stress change is that of rz component of the stress tensor at order n , which we denote as $\Delta\hat{\tau}_{rz,n}$. The stress changes are obtained from Hooke's law as

$$\Delta\hat{\tau}_{rz,n}^- = C_n^1 \frac{\mu^- \omega}{c_s^-} \left(J_{n-1}\left(\frac{\omega r}{c_s^-}\right) - \frac{nc_s^-}{\omega r} J_n\left(\frac{\omega r}{c_s^-}\right) \right), \quad (\text{B9a})$$

$$\Delta\hat{\tau}_{rz,n}^+ = -C_n^2 \frac{\mu^+ \omega}{c_s^+} \left(H_{n+1}^{(1)}\left(\frac{\omega r}{c_s^+}\right) - \frac{nc_s^+}{\omega r} H_n^{(1)}\left(\frac{\omega r}{c_s^+}\right) \right). \quad (\text{B9b})$$

Defining the one-sided impedance as the function relating stress changes and particle velocity immediately inside and outside of the ring fault, we have:

$$\hat{Z}_n^- \equiv \frac{\Delta\hat{\tau}_{rz,n}^-}{-i\omega\hat{w}_n^-} \Big|_{r=R} = \frac{i\mu^-}{c_s^-} \left(\frac{J_{n-1}(\omega R/c_s^-)}{J_n(\omega R/c_s^-)} - \frac{nc_s^-}{\omega R} \right), \quad (\text{B10a})$$

$$\hat{Z}_n^+ \equiv -\frac{\Delta\hat{\tau}_{rz,n}^+}{-i\omega\hat{w}_n^+} \Big|_{r=R} = -\frac{i\mu^+}{c_s^+} \left(\frac{H_{n+1}^{(1)}(\omega R/c_s^+)}{H_n^{(1)}(\omega R/c_s^+)} - \frac{nc_s^+}{\omega R} \right). \quad (\text{B10b})$$

We define slip on the ring fault as $\hat{\delta}_n \equiv \hat{w}_n^- - \hat{w}_n^+|_{r=R}$. It follows that the total impedance to ring fault slip, \hat{Z}_n , is

$$\hat{Z}_n \equiv \frac{\Delta\hat{\tau}_{rz,n}}{-i\omega\hat{\delta}_n} \Big|_{r=R} = \frac{\hat{Z}_n^- \hat{Z}_n^+}{\hat{Z}_n^+ + \hat{Z}_n^-}. \quad (\text{B11})$$

Note that $\Delta\hat{\tau}_{rz,n}|_{r=R} = \Delta\hat{\tau}_{rz,n}^-|_{r=R} = \Delta\hat{\tau}_{rz,n}^+|_{r=R}$.

For visualization, Equations B10a, B10b, and B11 are nondimensionalized with μ^-/c_s^- , and their magnitudes plotted numerically (Figure B1b) as a function of $\omega R/c_s^-$, μ^-/μ^+ , ρ^-/ρ^+ :

$$\tilde{Z}_n^- = i \left(\frac{J_{k-1}(\omega R/c_s^-)}{J_k(\omega R/c_s^-)} - \frac{nc_s^-}{\omega R} \right), \quad (\text{B12a})$$

$$\begin{aligned} \tilde{Z}_n^+ = & -i \left(\frac{\mu^+}{\mu^-} \right) \left(\frac{\mu^-}{\mu^+} \right)^{1/2} \left(\frac{\rho^+}{\rho^-} \right)^{1/2} \\ & \times \left(\frac{H_{k+1}^{(1)} \left[(\omega R/c_s^-)(\mu^-/\mu^+)^{1/2} (\rho^+/\rho^-)^{1/2} \right]}{H_k^{(1)} \left[(\omega R/c_s^-)(\mu^-/\mu^+)^{1/2} (\rho^+/\rho^-)^{1/2} \right]} - \frac{nc_s^+ (\mu^-)^{-1/2} (\rho^+)^{-1/2}}{\omega R (\mu^+)^{-1/2} (\rho^-)^{-1/2}} \right), \end{aligned} \quad (\text{B12b})$$

where crustal density, ρ , arises from combining shear modulus and wave speeds (e.g., $\rho^- = \mu^-/(c_s^-)^2$). In the analyses below, we derive the asymptotic approximations for the axisymmetric mode impedance \hat{Z}_0 to gain insight on how wave radiation impacts ring fault slip.

When the wavelength is small compared to the radius ($\omega R/c_s \gg 1$), the fault is effectively planar at the length scale of the wavelength and separates two semi-infinite half spaces. In this limit, we seek the large argument expansion of Equation B10b in $\omega R/c_s^+$ and obtain the radiation damping limit of impedance:

$$\hat{Z}_0^+ = -\frac{\mu^+}{c_s^+}. \quad (\text{B13})$$

Equation B13 is recognized as the radiation damping limit of impedance on one side of a planar bi-material fault for antiplane shear (Geubelle & Breitenfeld, 1997). Note that different from a planar fault, a ring fault does not have a radiation damping limit of impedance inward of the fault due to resonance associated with the length scale of the ring fault (Figure B1b).

When the wavelength is large compared to the radius ($\omega R/c_s \ll 1$), particle motions are approximately uniform within the caldera block. In this limit, we seek the Taylor series expansion of Equations B10a and B10b in $\omega R/c_s$ about zero and keep the leading terms:

$$\hat{Z}_0^- = \frac{-i\omega\rho^-R}{2}, \quad (\text{B14a})$$

$$\hat{Z}_0^+ = \frac{\mu^+}{-i\omega R \left(\log \left(\frac{\omega R}{2c_s^+} \right) + \gamma - i\pi/2 \right)}, \quad (\text{B14b})$$

where γ is the Euler–Mascheroni constant. The leading term of \hat{Z}_0^- represents the impedance due to caldera block inertia (Figure B1b). To see this, consider the caldera block inertia term, $m\ddot{\delta}$, (Equation C1) in the lumped parameter model (Kumagai et al., 2001; Wang et al., 2021). When $m\ddot{\delta}$ is normalized by the area of the ring fault, $2\pi RL$, the term has the unit of stress change. Examining the Fourier transform of the term,

$$\mathcal{F}\{m\ddot{\delta}\} = \frac{\pi R^2 L \rho^-(-i\omega)}{2\pi RL} (-i\omega\hat{\delta}) = \frac{-i\omega\rho^-R}{2} (-i\omega\hat{\delta}), \quad (\text{B15})$$

reveals that the leading term of $\hat{Z}_0^- (\omega R/c_s^- \rightarrow 0)$ indeed represents the impedance due to caldera block inertia. The leading term of \hat{Z}_0^+ can be interpreted as quasi-static effects modulated by waves (Figure B1b). $-\mu^+/(i\omega R)$ is of the form of quasi-static stiffness, with characteristic length scale R . The wave effects are indicated by the frequency dependence of the modifier, $\left(\log \left(\frac{\omega R}{2c_s^+} \right) + \gamma - i\pi/2 \right)^{-1}$.

In light of the above interpretations for \hat{Z}_0^- and \hat{Z}_0^+ , we can see that \hat{Z}_0 is dominated by caldera block inertia in the limit of $\omega R/c_s^- \ll 1$, and dominated by wave-mediated radiation damping in the limit of $\omega R/c_s^- \gg 1$ (Figure B1b).

In the $\omega R/c_s^- \gg 1$ limit, when $\mu^-/\mu^+ \ll 1$, $\hat{Z}_0 \rightarrow \hat{Z}_0^-$ and resonance effects within the ring fault are pronounced. Thus the impedance deviates significantly from that of shear slip on planar faults. When $\mu^-/\mu^+ \gg 1$, $\hat{Z}_0 \rightarrow \hat{Z}_0^+$ and resonance effects are subdued (Figure B1b, inset). Thus the impedance is well approximated with that of planar fault radiation damping with a pre-factor of two. Density contrast across the ring fault has similar effects as that of shear modulus contrast.

Some basaltic calderas exhibit trap-door faulting, which is well documented through geodetic, seismic observations on land (Amelung et al., 2000) and tsunami observations in the ocean (Sandanbata et al., 2022). During trap-door faulting, the caldera ring fault exhibits high-angle reverse slip at some azimuths, while the rest of the ring fault remains largely locked. This is kinematically similar to the initiation of a caldera collapse earthquake, where the ring fault initially ruptures a small azimuthal portion of the fault, albeit with the opposite sense of fault slip. In both cases, slip is asymmetric with regard to the azimuth of the ring fault. We can gain insight into the dynamics of asymmetric slip by constructing its impedance with those of the axisymmetric mode ($n = 0$; uniform slip rate at all azimuths) and the tilting mode ($n = 1$; upward slip rate on half of the azimuths and downward slip rate on the other half without net vertical translation of the caldera block) of slip.

Following the same procedure as for the axisymmetric mode of slip, we seek asymptotic approximations to the impedance of the tilting mode (Figure B1c). We find that, when the wavelength is small compared to the radius ($\omega R/c_s \gg 1$), impedance outside of the ring fault again takes the form of planar fault radiation damping:

$$\hat{Z}_1^+ = -\frac{\mu^+}{c_s^+}. \quad (\text{B16})$$

When the wavelength is large compared to ring fault radius ($\omega R/c_s \ll 1$), impedance takes the form of:

$$\hat{Z}_1^- = \frac{\mu^-}{-i\omega R}, \quad (\text{B17a})$$

$$\hat{Z}_1^+ = -\frac{\mu^+}{-i\omega R}. \quad (\text{B17b})$$

Equations B17a and B17b is recognized as quasi-static effects with fault stiffness μ/R , similar to that identified on planar faults (Dieterich, 1979). Quasi-static effects arise because asymmetric ring fault slip strains the caldera block, unlike in the axisymmetric case where motions within the block are dominated by vertical translation.

We can define the asymmetric slip as the average of the axisymmetric and tilting modes,

$$\begin{aligned} \hat{\delta}_{\text{asymmetric}}(\theta, \omega) &\equiv \frac{1}{2}(\hat{\delta}_0 + \hat{\delta}_1) \\ &= \frac{D(\omega)}{2}(1 + e^{i2\pi\theta}), \end{aligned} \quad (\text{B18})$$

yielding a slip profile sinusoidal in azimuth, smoothly varying between zero and a frequency-dependent amplitude, $D(\omega)$ (Figure B1d).

The ring fault stress change for the asymmetric slip is the superposition of the stress change due to the axisymmetric and tilting modes. Also recognizing that stress change is linear in slip rate via impedance, we have,

$$\begin{aligned} \Delta\hat{\tau}_{\text{asymmetric}}(\theta, \omega) &= \frac{1}{2}(\Delta\hat{\tau}_0(\omega) + \Delta\hat{\tau}_1(\omega)e^{i2\pi\theta}) \\ &= -i\omega \frac{D(\omega)}{2}(\hat{Z}_0(\omega) + \hat{Z}_1(\omega)e^{i2\pi\theta}), \end{aligned} \quad (\text{B19})$$

where subscript “ rz ” for stress change is omitted and subscript 0, 1 denote values for azimuthal order, n . We define the impedance for asymmetric slip as the frequency-dependent factor relating slip rate and stress change at $\theta = 0$, thus yielding:

$$\hat{Z}_{asymmetric} \equiv \frac{1}{2}(\hat{Z}_0(\omega) + \hat{Z}_1(\omega)).$$

Note that there is inherent ambiguity in defining the impedance for asymmetric slip, because $\hat{\delta}_{asymmetric}$ and $\Delta\hat{\tau}_{asymmetric}$ have different angular dependence. An alternative choice would be to define impedance using spatially averaged $\hat{\delta}_{asymmetric}$ and $\Delta\hat{\tau}_{asymmetric}$. The real and imaginary components of the nondimensionalized $\hat{Z}_{asymmetric}$ are plotted numerically (Figure B1e) for $\mu^-/\mu^+ = 1$ and $\rho^-/\rho^+ = 1$ (and the expressions that follow are specific to this assumption). We observe that, in the $\omega R/c_s^- \gg 1$ limit, the real component of $\hat{Z}_{asymmetric}$ dominates the imaginary component, and $\hat{Z}_{asymmetric}$ can be modeled with plane wave radiation damping, $-\mu^-/(2c_s^-)$. In the $\omega R/c_s^- \ll 1$ limit, $\hat{Z}_{asymmetric}$ has the following asymptotic limit:

$$\hat{Z}_{asymmetric} = \frac{2i\mu^-}{c_s^-} \left(1 + 4\gamma - 2\pi i + 4 \log \frac{\omega R}{2c_s^-} \right)^{-1} \left(\frac{\omega R}{c_s^-} \right)^{-3}. \quad (\text{B21})$$

Future work can utilize these frequency domain asymptotes for impedance to construct time domain lumped parameter models of trap-door faulting at caldera ring faults.

Appendix C: Seismic Wave Radiation Approximation in Lumped Model

Here we examine the effect of radiation damping on collapse dynamics, in the lumped parameter limit. For a rigid, cylindrical, caldera block surrounded by rigid crust, situated above an axisymmetric magma chamber filled with inviscid fluid, the momentum balance for the caldera block, with the initial equilibrium state subtracted, is (Kumagai et al., 2001):

$$m\ddot{\delta} = -2\pi RL\Delta\tau - \pi R^2\Delta p, \quad (\text{C1})$$

where R is the radius of the caldera block, L the height of the caldera block. δ , Δp , $\Delta\tau$ are the time dependent fault slip, chamber pressure change, and shear stress change, respectively. All changes are relative to initial states prior to collapse. The term on the left hand side is the caldera block inertia. The terms on the right hand side are changes in force due to the ring fault shear traction, and changes in force due to chamber pressure, respectively.

The pressure change can be related to fault slip via:

$$\Delta p = \frac{\pi R^2}{\beta V} \delta + \frac{\phi m_f}{\pi R^2} \dot{\delta} + \epsilon_p^m \rho_m c_p^m \dot{\delta}, \quad (\text{C2})$$

where ρ_m is magma density, β the combined compressibility of magma chamber wall and magma, V the magma chamber volume, m_f is the mass of magma in the reservoir, c_p^m is P-wave speed in the magma, and ϕ the fraction of total magma mass acting as inertial added mass impeding caldera block motion. ϵ_p^m is a dimensionless constant of order unity, encapsulating the importance of wave radiation. The first and second term on the right hand side are due to chamber storativity and inertia imparted by the magma, respectively (Wang et al., 2022). The third term is P-wave radiation damping in the magma.

The shear stress change is related to fault slip via:

$$\Delta\tau = \mathcal{T}(\delta) + \epsilon_s^r \rho_r c_s^r \dot{\delta}, \quad (\text{C3})$$

where ρ_r is the rock density, c_s^r the S-wave speed in the crust. The first term is the quasi-static stress change with nonlinear dependence on δ , determined a priori with static-dynamic friction:

$$\mathcal{T}(\delta) = \begin{cases} 0 & \text{for } \delta = 0 \\ (f_d - f_s)\sigma & \text{for } 0 < \delta < \delta_{\max}, \\ 2(f_d - f_s)\sigma & \text{for } \delta = \delta_{\max} \end{cases} \quad (C4)$$

where f_s is the static friction, f_d the dynamic friction, and σ the spatially uniform, constant ring fault normal stress. The second term on the right hand side of Equation C3 is S-wave radiation in the crust. Substituting Equations C2 and C3 into Equation C1, and grouping terms based on order of derivatives, we obtain:

$$m' \ddot{\delta} + (2\pi R L \epsilon_s^r \rho_r c_s^r + \pi R^2 \epsilon_p^m \rho_m c_p^m) \dot{\delta} + 2\pi R L \mathcal{T}(\delta) + \frac{\pi^2 R^4}{\beta V} \delta = 0, \quad (C5)$$

where $m' = m + \phi m_p \epsilon_s^r$ and ϵ_p^m can be estimated via the regime diagram (Figure 6a). $\epsilon_s^r = 1$ when $\omega R / c_s^r \gg 1$ and $\epsilon_s^r = 0$ when $\omega R / c_s^r \ll 1$. Similarly, $\epsilon_p^m = 1$ when $\omega H / c_p^m \gg 1$, and $\epsilon_p^m = 0$ when $\omega H / c_p^m \ll 1$. Note that the two radiation damping terms can be concisely written with the general expression, $\epsilon A \rho c \dot{\delta}$, with ϵ , A , ρ , and c correspond to relevant dimensionless number, surface area, density, and wave speed for P- or S-waves.

Data Availability Statement

All numerical simulations are performed using open source software SeisSol (Uphoff et al., 2022). Selected input files for benchmark and Kīlauea case simulations are available via Zenodo (Wang et al., 2024). Scripts for optimizing for SeisSol input parameters approximating the relaxation functions of Maxwell rheology and for demonstrating the effects of wave radiation on collapse earthquakes are also available via Zenodo (Wang & Dunham, 2024). GNSS data are available through UNAVCO archive (USGS Hawaiian Volcano Observatory (HVO), 2008). Accelerometer and broadband data are available through the Incorporated Research Institute for Seismology (IRIS) Data Management Center (U.S. Geological Survey, 1931; USGS Hawaiian Volcano Observatory (HVO), 1956). The catalog of very long period earthquakes analyzed in this study is presented in Table S1 of the Supporting Information S1.

Acknowledgments

The project is funded by a Stanford-USGS fellowship to T.A.W. and National Science Foundation Grants EAR-2040425 and EAR-2231849 to P.S. and E.M.D., respectively. Thanks to Carsten Uphoff for discussions on the implementation of Generalized Maxwell Bodies in SeisSol and William Ellsworth for discussions on complexities in earthquake nucleation. The manuscript improved from the thorough reviews of Meredith Townsend and Daniel Woodell. Lawrence Livermore National Laboratory is operated by Lawrence Livermore National Security, LLC, for the U.S. Department of Energy, National Nuclear Security Administration under Contract DE-AC5207NA27344. LLNL-JRNL-856488.

References

Amelung, F., Jónsson, S., Zebker, H., & Segall, P. (2000). Widespread uplift and ‘trapdoor’ faulting on Galapagos volcanoes observed with radar interferometry. *Nature*, 407(6807), 993–996. <https://doi.org/10.1038/35039604>

Anderson, K., & Johanson, I. (2022). Incremental caldera collapse at Kīlauea Volcano recorded in ground tilt and high-rate GNSS data, with implications for collapse dynamics and the magma system. *Bulletin of Volcanology*, 84(10), 1–26. <https://doi.org/10.1007/s00445-022-01589-x>

Anderson, K., Johanson, I., Patrick, M. R., Gu, M., Segall, P., Poland, M., et al. (2019). Magma reservoir failure and the onset of caldera collapse at Kīlauea Volcano in 2018. *Science*, 366(6470). <https://doi.org/10.1126/science.aaz1822>

Anderson, K. R., Shea, T., Lynn, K. J., Montgomery-Brown, E. K., Swanson, D. A., Patrick, M. R., et al. (2023). The 2018 eruption of Kīlauea: Insights, puzzles, and opportunities for volcano science. *Annual Review of Earth and Planetary Sciences*, 52(1). <https://doi.org/10.1146/annurev-earth-031621-075925>

Bowman, F. (2012). *Introduction to Bessel functions*. Courier Corporation.

Cattania, C., & Segall, P. (2021). Precursory slow slip and foreshocks on rough faults. *Journal of Geophysical Research: Solid Earth*, 126(4), e2020JB020430. <https://doi.org/10.1029/2020jb020430>

Christensen, R. (2012). *Theory of viscoelasticity: An introduction*. Elsevier.

Coppess, K. R., Dunham, E. M., & Almqvist, M. (2022). Ultra and very long period seismic signatures of unsteady eruptions predicted from conduit flow models. *Journal of Geophysical Research: Solid Earth*, 127(6), e2022JB024313. <https://doi.org/10.1029/2022jb024313>

Dawson, P., Chouet, B., Okubo, P., Villaseñor, A., & Benz, H. (1999). Three-dimensional velocity structure of the Kīlauea Caldera, Hawaii. *Geophysical Research Letters*, 26(18), 2805–2808. <https://doi.org/10.1029/1999gl1005379>

Day, S. M. (1982). Three-dimensional finite difference simulation of fault dynamics: Rectangular faults with fixed rupture velocity. *Bulletin of the Seismological Society of America*, 72(3), 705–727.

Dieterich, J. H. (1979). Modeling of rock friction: 1. Experimental results and constitutive equations. *Journal of Geophysical Research*, 84(B5), 2161–2168. <https://doi.org/10.1029/jb084b05p02161>

Dieterich, H. R., Diefenbach, A. K., Soule, S. A., Zoeller, M. H., Patrick, M. P., Major, J. J., & Lundgren, P. R. (2021). Lava effusion rate evolution and erupted volume during the 2018 Kīlauea lower east rift zone eruption. *Bulletin of Volcanology*, 83(4), 1–18. <https://doi.org/10.1007/s00445-021-01443-6>

Dingwell, D. B., & Webb, S. L. (1989). Structural relaxation in silicate melts and non-Newtonian melt rheology in geologic processes. *Physics and Chemistry of Minerals*, 16(5), 508–516. <https://doi.org/10.1007/bf00197020>

Dumbser, M., Käser, M., & Toro, E. F. (2007). An arbitrary high-order discontinuous Galerkin method for elastic waves on unstructured meshes—V. Local time stepping and p-adaptivity. *Geophysical Journal International*, 171(2), 695–717. <https://doi.org/10.1111/j.1365-246x.2007.03427.x>

Duputel, Z., & Rivera, L. (2019). The 2007 caldera collapse of Piton de la Fournaise volcano: Source process from very-long-period seismic signals. *Earth and Planetary Science Letters*, 527, 115786. <https://doi.org/10.1016/j.epsl.2019.115786>

Ellsworth, W., & Beroza, G. (1995). Seismic evidence for an earthquake nucleation phase. *Science*, 268(5212), 851–855. <https://doi.org/10.1126/science.268.5212.851>

Fichtner, A., & Tkalcic, H. (2010). Insights into the kinematics of a volcanic caldera drop: Probabilistic finite-source inversion of the 1996 Bárðarbunga, Iceland, earthquake. *Earth and Planetary Science Letters*, 297(3–4), 607–615. <https://doi.org/10.1016/j.epsl.2010.07.013>

Fontaine, F. R., Roult, G., Hejran, B., Michon, L., Ferrazzini, V., Barruol, G., et al. (2019). Very-and ultra-long-period seismic signals prior to and during caldera formation on La Réunion Island. *Scientific Reports*, 9(1), 1–15. <https://doi.org/10.1038/s41598-019-44439-1>

Geshi, N., Shimano, T., Chiba, T., & Nakada, S. (2002). Caldera collapse during the 2000 eruption of Miyakejima Volcano, Japan. *Bulletin of Volcanology*, 64(1), 55–68. <https://doi.org/10.1007/s00445-001-0184-z>

Geubelle, P. H., & Breitenfeld, M. S. (1997). Numerical analysis of dynamic debonding under anti-plane shear loading. *International Journal of Fracture*, 85(3), 265–282. <https://doi.org/10.1023/a:1007498300031>

Gudmundsson, M. T., Jónsdóttir, K., Hooper, A., Holohan, E. P., Halldórsson, S. A., Ófeigsson, B. G., et al. (2016). Gradual caldera collapse at Bárðarbunga volcano, Iceland, regulated by lateral magma outflow. *Science*, 353(6296). <https://doi.org/10.1126/science.aae8988>

James, M., Bagdassarov, N., Müller, K., & Pinkerton, H. (2004). Viscoelastic behaviour of basaltic lavas. *Journal of Volcanology and Geothermal Research*, 132(2–3), 99–113. <https://doi.org/10.1016/j.jvolgeores.2003.03408>

Krenz, L., Uphoff, C., Ulrich, T., Gabriel, A.-A., Abrahams, L. S., Dunham, E. M., & Bader, M. (2021). 3D acoustic-elastic coupling with gravity: The dynamics of the 2018 Palu, Sulawesi earthquake and tsunami. In *Proceedings of the international conference for high performance computing, networking, storage and analysis* (pp. 1–14).

Kumagai, H., Ohminato, T., Nakano, M., Ooi, M., Kubo, A., Inoue, H., & Oikawa, J. (2001). Very-long-period seismic signals and caldera formation at Miyake Island, Japan. *Science*, 293(5530), 687–690. <https://doi.org/10.1126/science.1062136>

Lai, V. H., Zhan, Z., Sandanbata, O., Brissaud, Q., & Miller, M. S. (2021). Inflation and asymmetric collapse at Kilauea summit during the 2018 eruption from seismic and infrasound analyses.

Lin, G., Shearer, P. M., Amelung, F., & Okubo, P. G. (2015). Seismic tomography of compressional wave attenuation structure for Kilauea Volcano, Hawaii. *Journal of Geophysical Research: Solid Earth*, 120(4), 2510–2524. <https://doi.org/10.1002/2014jb011594>

Lin, G., Shearer, P. M., Matza, R. S., Okubo, P. G., & Amelung, F. (2014). Three-dimensional seismic velocity structure of Mauna Loa and Kilauea volcanoes in Hawaii from local seismic tomography. *Journal of Geophysical Research: Solid Earth*, 119(5), 4377–4392. <https://doi.org/10.1002/2013jb010820>

Madariaga, R. (1976). Dynamics of an expanding circular fault. *Bulletin of the Seismological Society of America*, 66(3), 639–666. <https://doi.org/10.1785/bssa0660030639>

Mooney, H. M. (1974). Some numerical solutions for Lamb's problem. *Bulletin of the Seismological Society of America*, 64(2), 473–491. <https://doi.org/10.1785/bssa0640020473>

Neal, C. A., Brantley, S., Antolik, L., Babb, J., Burgess, M., Calles, K., et al. (2019). The 2018 rift eruption and summit collapse of Kilauea Volcano. *Science*, 363(6425), 367–374. <https://doi.org/10.1126/science.aav7046>

Okumura, S., Nakamura, M., Nakano, T., Uesugi, K., & Tsuchiyama, A. (2010). Shear deformation experiments on vesicular rhyolite: Implications for brittle fracturing, degassing, and compaction of magmas in volcanic conduits. *Journal of Geophysical Research*, 115(B6), B06201. <https://doi.org/10.1029/2009jb006904>

O'Reilly, O., Nordström, J., Kozdon, J. E., & Dunham, E. M. (2015). Simulation of earthquake rupture dynamics in complex geometries using coupled finite difference and finite volume methods. *Communications in Computational Physics*, 17(2), 337–370. <https://doi.org/10.4208/cicp.111013.120914a>

Patrick, M. R., Dietterich, H. R., Lyons, J. J., Diefenbach, A. K., Parcheta, C., Anderson, K., et al. (2019). Cyclic lava effusion during the 2018 eruption of Kilauea Volcano. *Science*, 366(6470). <https://doi.org/10.1126/science.aay9070>

Peltier, A., Staudacher, T., Bacheler, P., & Cayol, V. (2009). Formation of the April 2007 caldera collapse at Piton de La Fournaise volcano: Insights from GPS data. *Journal of Volcanology and Geothermal Research*, 184(1–2), 152–163. <https://doi.org/10.1016/j.jvolgeores.2008.09.009>

Pietruszka, A. J., & Garcia, M. O. (1999). The size and shape of Kilauea Volcano's summit magma storage reservoir: A geochemical probe. *Earth and Planetary Science Letters*, 167(3–4), 311–320. [https://doi.org/10.1016/s0012-821x\(99\)0036-9](https://doi.org/10.1016/s0012-821x(99)0036-9)

Pinkerton, H., & Norton, G. (1995). Rheological properties of basaltic lavas at sub-liquidus temperatures: Laboratory and field measurements on lavas from Mount Etna. *Journal of Volcanology and Geothermal Research*, 68(4), 307–323. [https://doi.org/10.1016/0377-0273\(95\)00018-7](https://doi.org/10.1016/0377-0273(95)00018-7)

Roman, A., & Lundgren, P. (2021). Dynamics of large effusive eruptions driven by caldera collapse. *Nature*, 592(7854), 392–396. <https://doi.org/10.1038/s41586-021-03414-5>

Saccorotti, G., Chouet, B., & Dawson, P. (2003). Shallow-velocity models at the Kilauea Volcano, Hawaii, determined from array analyses of tremor wavefields. *Geophysical Journal International*, 152(3), 633–648. <https://doi.org/10.1046/j.1365-246x.2003.01867.x>

Sandanbata, O., Watada, S., Satake, K., Kanamori, H., Rivera, L., & Zhan, Z. (2022). Sub-decadal volcanic tsunamis due to submarine trapdoor faulting at Sumisaki Caldera in the Izu–Bonin arc. *Journal of Geophysical Research: Solid Earth*, 127(9), e2022JB024213. <https://doi.org/10.1029/2022jb024213>

Savage, J. (1972). Relation of corner frequency to fault dimensions. *Journal of Geophysical Research*, 77(20), 3788–3795. <https://doi.org/10.1029/jb077i020p03788>

Segall, P., & Anderson, K. (2021). Repeating caldera collapse events constrain fault friction at the kilometer scale. *Proceedings of the National Academy of Sciences of the United States of America*, 118(30). <https://doi.org/10.1073/pnas.2101469118>

Segall, P., Anderson, K., Pulvirenti, F., Wang, T. A., & Johanson, I. (2020). Caldera collapse geometry revealed by near-field GPS displacements at Kilauea Volcano in 2018. *Geophysical Research Letters*, 47(15), e2020GL088867. <https://doi.org/10.1029/2020gl088867>

Segall, P., Anderson, K., & Wang, T. A. (2022). Could Kilauea's 2020 post caldera-forming eruption have been anticipated? *Geophysical Research Letters*, 49(15), e2022GL099270. <https://doi.org/10.1029/2022gl099270>

Segall, P., Matthews, M. V., Shelly, D. R., Wang, T. A., & Anderson, K. R. (2024). Stress-driven recurrence and precursory moment-rate surge in caldera collapse earthquakes. *Nature Geoscience*, 17(3), 1–6. <https://doi.org/10.1038/s41561-023-01372-3>

Shelly, D. R., & Thelen, W. A. (2019). Anatomy of a caldera collapse: Kilauea 2018 summit seismicity sequence in high resolution. *Geophysical Research Letters*, 46(24), 14395–14403. <https://doi.org/10.1029/2019gl085636>

Tepp, G., Hotovec-Ellis, A., Shiro, B., Johanson, I., Thelen, W., & Haney, M. M. (2020). Seismic and geodetic progression of the 2018 summit caldera collapse of Kilauea Volcano. *Earth and Planetary Science Letters*, 540, 116250. <https://doi.org/10.1016/j.epsl.2020.116250>

Ulrich, T., Gabriel, A.-A., & Madden, E. H. (2022). Stress, rigidity and sediment strength control megathrust earthquake and tsunami dynamics. *Nature Geoscience*, 15(1), 67–73. <https://doi.org/10.1038/s41561-021-00863-5>

Uphoff, C. (2020). Flexible model extension and optimisation for earthquake simulations at extreme scales (Unpublished doctoral dissertation). Technische Universität München.

Uphoff, C., & Bader, M. (2016). Generating high performance matrix kernels for earthquake simulations with viscoelastic attenuation. In *2016 international conference on high performance computing & simulation (HPCS)* (pp. 908–916).

Uphoff, C., Krenz, L., Ulrich, T., Wolf, S., Knoll, A., David, S., et al. (2022). SeisSol [Computer software]. <https://github.com/SeisSol/SeisSol>

U.S. Geological Survey. (1931). United States national strong-motion network [Dataset]. *International Federation of Digital Seismograph Networks*. <https://doi.org/10.7914/SN/NP>

USGS Hawaiian Volcano Observatory (HVO). (1956). Hawaiian volcano observatory network [Dataset]. *International Federation of Digital Seismograph Networks*. <https://doi.org/10.7914/SN/HV>

USGS Hawaiian Volcano Observatory (HVO). (2008). Hawaii global positioning system network [Dataset]. *GAGE Facility, GPS/GNSS Observations*. <https://doi.org/10.7283/T5RR1WGN>

Wang, T. A., Coppess, K. R., Segall, P., Dunham, E. M., & Ellsworth, W. (2022). Physics-based model reconciles caldera collapse induced static and dynamic ground motion: Application to Kīlauea 2018. *Geophysical Research Letters*, 49(8), e2021GL097440. <https://doi.org/10.1029/2021GL097440>

Wang, T. A., & Dunham, E. M. (2024). Scripts for optimizing for SeisSol input parameters approximating the relaxation functions of Maxwell rheology and for demonstrating the effects of wave radiation on collapse earthquakes [Computer software]. Zenodo. <https://doi.org/10.5281/zenodo.10129848>

Wang, T. A., Krenz, L., Abrahams, L. S., & Yoder, M. R. (2024). Input files to SeisSol simulations of caldera collapse earthquakes [Simulation input]. Zenodo. <https://doi.org/10.5281/zenodo.10128043>

Wang, T. A., Segall, P., Hotovec-Ellis, A. J., Anderson, K. R., & Cervelli, P. F. (2023). Ring fault creep drives volcano-tectonic seismicity during caldera collapse of Kīlauea in 2018. *Earth and Planetary Science Letters*, 618, 118288. <https://doi.org/10.1016/j.epsl.2023.118288>

Wang, T. A., Zheng, Y., Pulvirenti, F., & Segall, P. (2021). Post-2018 caldera collapse re-inflation uniquely constrains Kīlauea's magmatic system. *Journal of Geophysical Research: Solid Earth*, 126(6), e2021JB021803. <https://doi.org/10.1029/2021jb021803>

Webb, S. L., & Dingwell, D. B. (1990). The onset of non-Newtonian rheology of silicate melts: A fiber elongation study. *Physics and Chemistry of Minerals*, 17(2), 125–132. <https://doi.org/10.1007/bf00199663>

Williams, D. M., Avery, V. F., Coombs, M. L., Cox, D. A., Horwitz, L. R., McBride, S. K., et al. (2020). US geological survey 2018 Kīlauea Volcano eruption response in Hawai'i—After-action review. (Technical Report). US Geological Survey.